

Wavepacket Dynamics of the Axially Chiral Molecule Cl–O–O–Cl under Coherent Radiative Excitation and Including Electroweak Parity Violation

Published as part of *The Journal of Physical Chemistry A* virtual special issue “Spectroscopy and Dynamics of Medium-Sized Molecules and Clusters: Theory, Experiment, and Applications”.

Robert Prentner,^{*,†,‡} Martin Quack,^{*,†} Jürgen Stohner,[§] and Martin Willeke^{†,||}

[†]Laboratory for Physical Chemistry, ETH Zürich, CH-8093 Zürich, Switzerland

[‡]Chair for Philosophy, ETH Zürich, CH-8092 Zürich, Switzerland

[§]Institute for Chemistry and Biological Chemistry, Zürich University for Applied Sciences, Campus Reidbach, CH-8840 Wädenswil, Switzerland

^{||}Department of Materials, ETH Zürich, CH-8093 Zürich, Switzerland

Supporting Information

ABSTRACT: We report detailed calculations of the quantum wavepacket dynamics of Cl–O–O–Cl, which serves as a prototype molecule for the stereomutation dynamics of an axially chiral molecule. We include the effects both from electroweak parity violation and from the interaction with a coherent monochromatic laser field. We use the quasideiabatic channel reaction path Hamiltonian approach to approximately solve the six-dimensional Schrödinger equation describing the vibrational motion, including rotation by an effective Hamiltonian. We calculate time-dependent wave functions based on the time-dependent Schrödinger equation. We study stereomutation dynamics due to tunneling motion and laser-induced population transfer and show results on efficient methods for selectively populating single molecular states in chiral molecules by frequency-modulated laser pulses. We also discuss laser-induced stereomutation (LISM) and a process that may be called resonance Raman induced stereomutation (RRISM). The results are discussed in relation to current experimental attempts to measure the parity violating energy difference $\Delta_{\text{pv}}E$ between the enantiomers of chiral molecules. Furthermore, we show detailed quantitative simulations of a selection of well-defined parity levels in chiral molecules (“parity isomers”) that form the basis of a possible measurement of $\Delta_{\text{pv}}E$ by the time evolution of parity.

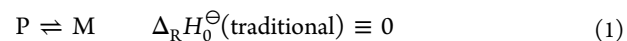


1. INTRODUCTION

Molecular chirality has been a central aspect of stereochemistry for more than a century.^{1–6} The quantum dynamics of chiral molecules has remained an important subject of physics and chemistry ever since its first treatment shortly after the development of quantum mechanics.⁷ It is highly relevant for a broad range of studies such as investigations into the foundations of physics, symmetries and reaction dynamics,^{8–10} spectroscopy,^{11–13} or the evolution of biologically important molecules such as proteins, DNA, or sugars.^{14–18} Even pharmacology has to deal with a wide range of chiral substances and drugs, with nearly two-thirds of all worldwide drugs being chiral.¹⁹ There has also been recent interest in the coherent preparation of separate enantiomers from racemic mixtures and related problems.^{20,21}

According to the traditional point of view, based on the assumption of rigorous space inversion symmetry related to parity conservation in physics, the two enantiomers of chiral molecules would be exactly equivalent energetically. Their ground states and all corresponding excited quantum states

would have the same energies. The reaction enthalpy $\Delta_{\text{R}}H_0^\ominus$ for the stereomutation reaction (1) converting the P enantiomer of an axially chiral molecule into the M enantiomer would be exactly zero by symmetry.



However, the discovery of parity violation in nuclear and high-energy physics^{22–30} has resulted in a fresh look at molecular chirality as well.^{31,32} Indeed, one can expect a small parity violating energy difference $\Delta_{\text{pv}}E_0$ to exist between the ground state energies of chiral molecules equivalent to a nonzero reaction enthalpy

$$\Delta_{\text{R}}H_0^\ominus(\text{real}) = \Delta_{\text{pv}}H_0^\ominus = N_{\text{A}}\Delta_{\text{pv}}E_0 \quad (2)$$

Received: September 14, 2015

Revised: October 29, 2015

Published: October 29, 2015

Qualitative and semiquantitative estimates for $\Delta_{\text{pv}}E_0$ have existed for quite some time,^{31–35} and the effects from parity violation were also proven in atomic spectroscopy.^{36–41} However, so far no experiment has been successful in measuring $\Delta_{\text{pv}}E_0$, because of its small magnitude.

Recent progress in theory has shown $\Delta_{\text{pv}}E$ to be 1–2 orders of magnitude larger than previously anticipated for typical benchmark molecules and thus has greatly improved the outlook to detect molecular parity violation^{42–49} (see also ref 50 for most recent results and further references). There have been several proposals for experiments (and also some attempts) to detect effects from molecular parity violation.^{51–59} One of these schemes is actually able to directly measure $\Delta_{\text{pv}}E$ ⁵⁴ by using a spectroscopic detection of the time dependence of parity and more generally intermediate spectroscopic levels of well-defined parity. In the context of preparing for such experiments our theoretical investigation was undertaken.

In the present work we concentrate on the detailed quantum dynamics of single chiral molecules with C_2 symmetry of the X–Y–Y–X type (Figure 1) such as hydrogen peroxide,

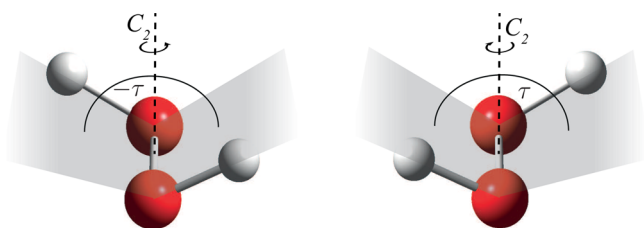


Figure 1. Chiral enantiomers of molecules of type X–Y–Y–X. The torsional angle τ is the angle between the X–Y–Y and Y–Y–X plane, respectively. A C_2 symmetry axis symmetrically bisects τ and is orthogonal to the line connecting the Y atoms.

H–O–O–H, or dichlorine dioxide, Cl–O–O–Cl, where in addition to the Born–Oppenheimer potential energy surface the effect of electroweak parity violation is taken into account.^{12,44,47,50,60}

For these molecules one can distinguish two limiting cases. In the first case, such as in hydrogen peroxide, the quantum dynamics is dominated by the large tunneling splittings (e.g., see ref 61, $\Delta E_{\pm} \approx (hc) 10 \text{ cm}^{-1}$) and thus the much smaller effects from parity violating potentials $V_{\text{pv}}/(hc)$ (on the order of $10^{-12\pm 2} \text{ cm}^{-1}$) are negligible. The molecular eigenstates have an almost exactly defined parity. In the second case the tunneling splittings for the hypothetical symmetrical potential (ΔE_{\pm}^0 , excluding parity violating effects) in the ground state (superscript 0) are much smaller than the parity violating energy difference between enantiomers $\Delta_{\text{pv}}E$; thus

$$\Delta_{\text{pv}}E_0 \gg \Delta E_{\pm}^0 \quad (3)$$

Such a case applies to Cl–O–O–Cl,⁶² the main topic of the present investigation, and similarly to Cl–S–S–Cl⁶³ and in fact all stable chiral molecules.^{8,9}

At higher vibrational excitations, however, tunneling splittings $\Delta E_{\pm}^{(n)}$ in excited states n can become much larger than $\Delta_{\text{pv}}E^{(n)}$ and thus one observes “tunneling switching” to excited eigenstates of well-defined parity.^{62,64} These cases are particularly interesting, as they allow for a measurement of parity violation by parity selection and subsequent study of the time evolution of parity.⁵⁴ In the present work we present

results on time-dependent wavepacket dynamics for both limiting cases. The outline is briefly as follows:

In section 2 we report on the general theoretical model used and then show in section 3 results for different numerical simulations of a chiral molecule under the influence of parity violation and laser irradiation. In subsections 3.1–3.4 we will report our findings on several limiting cases of the quantum dynamics of Cl–O–O–Cl that include population transfer and tunneling motion. Subsection 3.5 is devoted to the simulation of a possible experiment to measure the parity violating energy difference in a chiral molecule. Cl–O–O–Cl serves as realistic molecule and our simulations can thus be considered a (theoretical) proof of principle for such an experiment. Finally, we discuss our findings and give a brief outlook in section 4.

A preliminary account of the present work was given in ref 65.

2. THEORETICAL MODEL

2.1. Stationary States and Parity Violation. The quantum dynamics of a molecule are described by the time-dependent Schrödinger equation,

$$i\hbar \frac{\partial \Psi(\mathbf{x}, t)}{\partial t} = \hat{H}(\mathbf{x}, t) \Psi(\mathbf{x}, t) \quad (4)$$

with the Hamilton operator $\hat{H}(\mathbf{x}, t)$ and the time-dependent wave function $\Psi(\mathbf{x}, t)$, $\hbar = h/(2\pi)$ is the reduced Planck constant and the imaginary unit $i = \sqrt{-1}$. The time-dependent wave function can be written as a superposition of time-independent stationary state wave functions $\varphi(\mathbf{x})$ of the isolated molecule which only depend on the spatial coordinates \mathbf{x} , with time-dependent coefficients $b_k(t)$ accounting for the time dependence of the quantum state:

$$\Psi(\mathbf{x}, t) = \sum_{k=1}^{\infty} b_k(t) \varphi(\mathbf{x}) \quad (5)$$

The wave functions $\varphi(\mathbf{x})$ are eigenfunctions of the molecular time-independent Hamilton operator and solve the time-independent Schrödinger equation

$$\hat{H}_{\text{mol}}(\mathbf{x}) \varphi_k(\mathbf{x}) = E_k \varphi_k(\mathbf{x}) \quad (6)$$

To arrive at eigenvalues and eigenfunctions, we use here the quadiabatic channel reaction path Hamilton (RPH) approximation^{61,62,65–68} to obtain an approximate numerical expression for the molecular Hamiltonian. The vibrational Hamilton operator in the RPH approximation takes the following form (with total angular momentum $J = 0$):

$$\hat{H}_{\text{mol}}(\mathbf{x}) = \hat{H}_{J=0}^{\text{RPH}}(\hat{\mathbf{P}}, \mathbf{Q}, \hat{p}, \tau) = \hat{H}_{\mathbf{Q}}(\hat{\mathbf{P}}, \mathbf{Q}; \tau) + \hat{H}_{\tau}(\hat{p}, \tau) \quad (7)$$

where the total coordinate space \mathbf{x} (molecular frame) is spanned by a reaction path coordinate τ (Figure 1) and $3N - 7$ coordinates \mathbf{Q} represented as normal coordinates; \hat{p} and $\hat{\mathbf{P}}$ are the corresponding momentum operators. For details we refer to refs 61, 62, and 65–68 (see also refs 69–73). The reaction path was determined by optimizing all internal coordinates for successive values of the torsional coordinate τ (“clamped coordinate approach”).

The right-hand side of eq 7 is a sum of two terms, a Hamilton operator $\hat{H}_{\tau}(\hat{p}, \tau)$, only dependent on the reaction path coordinate τ and its conjugate momentum \hat{p} , and a term $\hat{H}_{\mathbf{Q}}(\hat{\mathbf{P}}, \mathbf{Q}; \tau)$, which is only parametrically dependent on τ .

Therefore, we can use an adiabatic ansatz for calculating the molecular eigenfunctions. We treat the motion along the normal coordinates as harmonic, which leads to an effective 1-dimensional Schrödinger equation in the reaction path coordinate τ :

$$\left(\frac{1}{2}\hat{p}I_{\text{eff}}(\tau)^{-1}\hat{p} + V_{\text{el}}(\tau) + V_{\text{corr}}(\tau) - E\right)\varphi(\tau) = 0 \quad (8)$$

with the effective moment of inertia I_{eff} .^{61,67,68} The total potential energy is a sum of the electronic potential energy along the reaction coordinate, $V_{\text{el}}(\tau)$, and a correction $V_{\text{corr}}(\tau)$ arising from the coordinate transformation from Cartesian coordinates \mathbf{x} to (τ, \mathbf{Q}) ^{74–77} and the adiabatic coupling of the normal modes along \mathbf{Q} to the reaction path (consisting mainly of zero-point energy effects but also including Coriolis-type couplings). As the resulting effective 1-dimensional potentials can be considered as quadiabatic reaction channels, the total effective potential may be called the (quasi)adiabatic channel potential in the spirit of refs 71–73.

Equation 8 is finally solved numerically using a discrete variable representation (DVR) on an equidistant grid.^{61,67,78–86} We used a modified version of the original RPH program of refs 61 and 67 for determining very small tunneling splittings.^{62,87} The original program made use of filtering the molecular data by periodic series at the end of the calculation. However, in the new version of the program the positions, potential energies and force fields calculated *ab initio* are fitted to a sin or cos series before the actual calculation of the RPH potential, whereas in the previous version a “filtering” by fitting the potentials and harmonic frequencies to a ten-dimensional cos series was done at the last steps of the computation.^{62,87} We could increase the stability and convergence of the results (for a comparison between the RPH version used in this work and that in ref 62, one can consult the Supporting Information). Table 1 gives an overview of the newly calculated vibrational energy levels for Cl–O–O–Cl (columns 2 and 4) compared to the previously calculated results from ref 62 (columns 3 and 5). The absolute energies change only slightly, whereas the ratios of the tunneling splittings change up to 1 order of magnitude for the smallest values of the torsional quantum number ν . These are, however, much less than the parity violating energy and hardly influence the overall quantum dynamics, as will be discussed in sections 3.1–3.5.

The total Hamilton operator from eq 4 typically consists of further expressions. In our case these are a potential accounting for the parity violating weak interaction (the “parity violating potential”) and the interaction of the molecule with a coherent optical field in the dipole approximation. The total Hamiltonian then reads

$$\hat{H}(\mathbf{x}, t) = \hat{H}_{\text{mol}}(\mathbf{x}) + V_{\text{pv}}(\mathbf{x}) - \vec{\mu}(\mathbf{x}) \cdot \vec{E}(\mathbf{x}, t) \quad (9)$$

Having solved the eigenproblem of the first part of the molecular Hamiltonian in eq 9 within the RPH approximation, we could treat the very small parity violating potentials V_{pv} by perturbation theory.^{8,12,48,54,93} The parity conserving potential V_{el} was calculated with *ab initio* quantum chemical methods.⁸⁸ Electron correlation was included using the second-order Møller–Plesset perturbation theory (MP2) with an aug-cc-pVTZ basis set. All energies, molecular geometries, force fields, and electric dipole moments were calculated along the torsional angle τ every 10°, and all other coordinates were optimized. Similarly, the parity violating potential V_{pv} has been calculated

Table 1. Bound Torsional Eigenstates ($J = 0$) with $\nu \leq 14$ in Cl–O–O–Cl in High Barrier Notation^a

ν	$\tilde{\nu}_\nu(\text{Å}^+)/\text{cm}^{-1}$		$\Delta\tilde{\nu}_\nu = [\tilde{\nu}_\nu(\text{Å}^-) - \tilde{\nu}_\nu(\text{Å}^+)]/\text{cm}^{-1}$	
0	0.0 ^b	0.0 ^c	6.77×10^{-24}	6.7×10^{-25}
1	122.2116	123.6	4.53×10^{-22}	5.1×10^{-23}
2	243.1360	245.4	1.56×10^{-20}	2.0×10^{-21}
3	362.3660	364.9	3.68×10^{-19}	5.0×10^{-20}
4	479.4309	481.9	6.60×10^{-18}	9.3×10^{-19}
5	593.8252	596.0	9.48×10^{-17}	1.4×10^{-17}
6	705.0087	706.8	1.13×10^{-15}	1.7×10^{-16}
7	812.3816	813.8	1.25×10^{-14}	2.8×10^{-15}
8	915.2396	916.5	7.79×10^{-13}	6.1×10^{-13}
9	1012.7046	1014.0	3.71×10^{-10}	3.1×10^{-10}
10	1103.5946	1105.3	2.02×10^{-7}	1.7×10^{-7}
11	1186.0779	1188.2	1.21×10^{-4}	1.0×10^{-4}
12	1256.1109	1258.5	0.1066	0.08
13	1284.5158	1290.5	16.0465	12.6
14	1312.9167	1316.4	19.5574	19.5

^aIn columns 2 and 4 we give the values from the present work, and in columns 3 and 5 we give the results from ref 62 for comparison. The tunneling splittings are extremely small up to $\nu \approx 9$. The horizontal line after $\nu = 7$ indicates the point where the tunneling splittings in both versions reach the same order of magnitude. The tunneling splittings are calculated for the hypothetical symmetric potential. ^bGround state at 1507.51 cm⁻¹. ^cGround state at 1504.64 cm⁻¹.

along τ with the RPA/6-311+G(3df) method⁴⁷ as described in ref 62, which is also in good agreement with more recent calculations at the coupled cluster (CCSD(T)) level.^{50,60} The potential V_{pv} is many orders of magnitude smaller than the quadiabatic channel RPH potential, which justifies the perturbation treatment. Figure 2 shows a comparison between

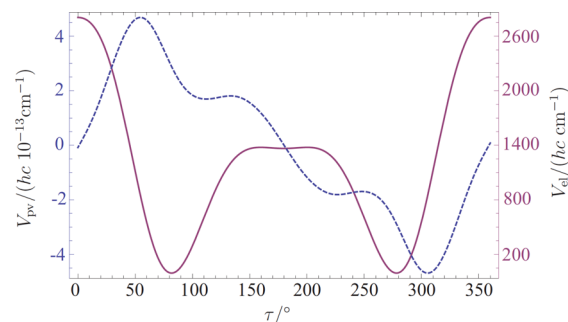


Figure 2. Parity violating potential V_{pv} (RPA/6-311+G(3df), dotted line, left-hand ordinate scale)⁶² and the electronic Born–Oppenheimer potential V_{el} (MP2/aug-cc-pVTZ, full line, right-hand ordinate scale) along the torsional coordinate τ . V_{pv} is by orders of magnitude smaller than the electronic potential and may be thus treated by perturbation theory.

the electronic Born–Oppenheimer potential and the parity violating potential along the reaction coordinate.

In the case of Cl–O–O–Cl the bound states of the molecular, symmetric reaction path Hamiltonian can be reordered in tunneling pairs; i.e., all torsional eigenstates can be numbered by a torsional quantum number ν and an indicator \pm giving the parity of the respective tunneling eigenstate (“high barrier notation”). The tunneling splittings $\Delta\tilde{\nu}_\nu = \tilde{\nu}_\nu(\text{Å}^-) - \tilde{\nu}_\nu(\text{Å}^+)$ are very small then, whereas the

splittings between states with different ν are comparatively large. In the simplest case one can treat the perturbation for two states using a 2×2 matrix.^{8,54} More generally, one can build a block diagonal matrix

$$\mathbf{H} = \begin{pmatrix} H_1 & 0 & \dots & 0 \\ 0 & H_2 & \dots & 0 \\ \vdots & & \ddots & \vdots \\ 0 & \dots & \dots & H_n \end{pmatrix} \quad (10)$$

composed of n matrices \mathbf{H}_ν

$$\mathbf{H}_\nu = hc \begin{pmatrix} \tilde{\nu}_\nu(A^+) & \tilde{V}_\nu^{(pv)} \\ \tilde{V}_\nu^{(pv)} & \tilde{\nu}_\nu(A^-) \end{pmatrix} \quad (11)$$

with the matrix element of the parity violating contribution, $hc\tilde{V}_\nu^{(pv)} = \langle \varphi_\nu^+ | V_{pv} | \varphi_\nu^- \rangle$. By diagonalization we find the new eigenenergies of the system under the influence of parity violation. For each quantum number ν we find two eigenstates that diagonalize one block entry given in eq 11. These two eigenstates shall be denoted as l and u states (for lower and upper) belonging to the quantum number ν . One can distinguish two limiting cases:

$$\tilde{\nu}_\nu(l,u) = \frac{1}{2}(\tilde{\nu}_\nu(A^+) + \tilde{\nu}_\nu(A^-)) \pm \frac{1}{2}(4(\tilde{V}_\nu^{(pv)})^2 + \Delta\tilde{\nu}_\nu^2)^{1/2} \quad (12)$$

$$\approx \begin{cases} \frac{1}{2}(\tilde{\nu}_\nu(A^+) + \tilde{\nu}_\nu(A^-)) \pm \tilde{V}_\nu^{(pv)} \stackrel{\text{def}}{=} \tilde{\nu}_\nu(P,M) & \text{if } \tilde{V}_\nu^{(pv)} \gg \Delta\tilde{\nu}_\nu \\ \tilde{\nu}_\nu(A^+) \text{ or } \tilde{\nu}_\nu(A^-) & \text{if } \Delta\tilde{\nu}_\nu \gg \tilde{V}_\nu^{(pv)} \end{cases} \quad (13)$$

with eigenstates

$$\varphi_\nu^{l,u} \approx \begin{cases} \frac{1}{\sqrt{2}}(\varphi_\nu^+ \pm \varphi_\nu^-) \stackrel{\text{def}}{=} \varphi_\nu^{P,M} & \text{if } \tilde{V}_\nu^{(pv)} \gg \Delta\tilde{\nu}_\nu \\ \varphi_\nu^+ \text{ or } \varphi_\nu^- & \text{if } \Delta\tilde{\nu}_\nu \gg \tilde{V}_\nu^{(pv)} \end{cases} \quad (14)$$

In the case of Cl–O–O–Cl we find that for states with $\nu \leq 7$ parity violation is dominant over tunneling (i.e., $\tilde{V}_\nu^{(pv)} \gg \Delta\tilde{\nu}_\nu$), whereas for $\nu \geq 9$ tunneling is dominant over parity violation. Table 2 shows a comparison between parity violation and tunneling splitting of the symmetric potential as a function of torsional quantum number ν .

The eigenstates represent chiral states $\varphi_\nu^{P,M}$ for the torsional ground state and modest torsional excitations, where parity violation is dominant ($\tilde{V}_\nu^{(pv)} \gg \Delta\tilde{\nu}_\nu$), and delocalized parity eigenstates $\varphi_\nu^{+,-}$ for higher torsional excitations, where tunneling is dominant ($\tilde{V}_\nu^{(pv)} \ll \Delta\tilde{\nu}_\nu$, Figure 3). This change of character from chiral to parity eigenstates has been called “tunneling switching”,⁶² which also occurs in other physical situations with slightly asymmetric potentials such as in *o*-D-phenol.⁶⁴ For exceedingly small tunneling splittings, the splitting between two chiral states is characterized by the parity violating energy difference $\Delta_{pv}E$ with

$$|\Delta_{pv}E| = |\langle \varphi^M | V_{pv} | \varphi^M \rangle - \langle \varphi^P | V_{pv} | \varphi^P \rangle| \\ = 2|\langle \varphi^M | V_{pv} | \varphi^M \rangle| = 2|\langle \varphi^+ | V_{pv} | \varphi^+ \rangle| \quad (15)$$

Note that the absolute value of the parity violating energy difference $\Delta_{pv}E$ equals twice the absolute value of the matrix element of the parity violating potential V_{pv} (assumed to be real) in the limiting case where the tunneling splittings are

Table 2. Parity Violation $2V_\nu^{(pv)} = 2\langle \varphi_\nu^+ | V_{pv} | \varphi_\nu^- \rangle$ (RPA/6-311+G(3df)) Compared to Tunneling Splitting $\Delta\tilde{\nu}_\nu = \tilde{\nu}_\nu(A^-) - \tilde{\nu}_\nu(A^+)$ (Calculated for the Symmetrical Case from the RPH Calculation with MP2/aug-cc-pVTZ) in Cl–O–O–Cl^a

ν	$2V_\nu^{(pv)}/(hc \text{ cm}^{-1})$	$\Delta\tilde{\nu}_\nu/\text{cm}^{-1}$	$\tilde{\nu}_\nu(u) - \tilde{\nu}_\nu(l)/\text{cm}^{-1}$
0	5.75×10^{-13}	6.77×10^{-24}	5.75×10^{-13}
1	5.69×10^{-13}	4.53×10^{-22}	5.69×10^{-13}
2	5.64×10^{-13}	1.56×10^{-20}	5.64×10^{-12}
3	5.58×10^{-13}	3.68×10^{-19}	5.58×10^{-13}
4	5.52×10^{-13}	6.60×10^{-18}	5.52×10^{-13}
5	5.46×10^{-13}	9.48×10^{-17}	5.46×10^{-13}
6	5.40×10^{-13}	1.13×10^{-15}	5.40×10^{-13}
7	5.34×10^{-13}	1.25×10^{-14}	5.34×10^{-13}
8	5.26×10^{-13}	7.79×10^{-13}	9.40×10^{-13}
9	5.17×10^{-13}	3.71×10^{-10}	3.71×10^{-10}
10	5.06×10^{-13}	2.02×10^{-7}	2.02×10^{-7}
11	4.90×10^{-13}	1.21×10^{-4}	1.21×10^{-4}
12	4.52×10^{-13}	0.11×10^{-1}	0.11×10^{-1}

^aShown in the right column is the splitting between the two eigenstates including the electroweak perturbation denoted as $\tilde{\nu}_\nu(u) - \tilde{\nu}_\nu(l)$ according to eq 13. One can see the effect of tunneling switching for $\nu \geq 9$.

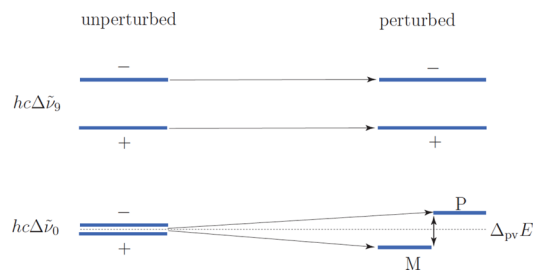


Figure 3. Eigenstates for Cl–O–O–Cl after perturbation showing tunneling switching.⁶² For small torsional quantum numbers, $\nu \leq 7$, the parity violating energy difference $\Delta_{pv}E$ is much larger than the tunneling splitting $hc\Delta\tilde{\nu}_\nu$. Eigenstates thus represent well-localized molecular states separated by $\Delta_{pv}E$. For higher torsional excitations, $\nu \geq 9$, $hc\Delta\tilde{\nu}_\nu$ is much larger than $\Delta_{pv}E$. Eigenstates then represent delocalized parity eigenstates separated by $hc\Delta\tilde{\nu}_\nu$.

small compared to parity violation. By comparing $|\Delta_{pv}E|$ and $|\Delta E_{\pm}|$, one can determine where the eigenstates change from localized to delocalized states (see also Table 2, where the $\Delta\tilde{\nu} = E/hc$ are given). All torsional vibrational eigenstates of Cl–O–O–Cl below 2500 cm^{-1} with the effects of V_{pv} included are shown in Figure 4.

Furthermore, rovibrational levels have been calculated approximately by using an effective rotational Hamilton operator implemented in the program WANG of ref 89. The rotational Hamiltonian for asymmetric tops in a S -reduced form⁹⁰ can be written as

$$\hat{H}_{\text{rot}}^{\text{eff}} = A\hat{J}_z^2 + B\hat{J}_x^2 + C\hat{J}_y^2 \\ - D_J\hat{J}^4 - D_{JK}\hat{J}_z^2\hat{J}^2 - D_K\hat{J}_z^4 \\ + d_J\hat{J}^2(\hat{J}_+^2 + \hat{J}_-^2) + d_2(\hat{J}_+^4 + \hat{J}_-^4) \\ + H_J\hat{J}^6 + H_{JK}\hat{J}_z^4\hat{J}^2 + H_{KJ}\hat{J}_z^2\hat{J}^4 + H_K\hat{J}_z^6 \\ + h_J\hat{J}^4(\hat{J}_+^2 + \hat{J}_-^2) + h_2\hat{J}^2(\hat{J}_+^4 + \hat{J}_-^4) + h_3(\hat{J}_+^6 + \hat{J}_-^6) \quad (16)$$

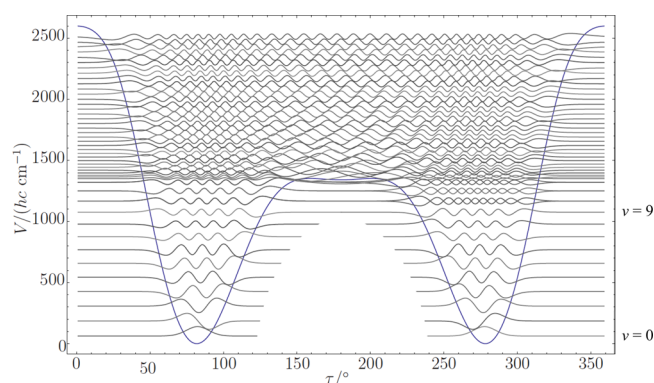


Figure 4. Bound eigenstates of the quadiabatic ground state channel ($J = 0$), drawn at their energies after perturbation. For states with energies below 1000 cm^{-1} ($\nu < 9$) the parity violating energy difference is much larger than the tunneling splitting. Thus, these eigenfunctions are localized, which is indicated by not being drawn over the whole space. At higher excitations the eigenfunctions are effectively delocalized over both wells and thus represented continuously over all values of τ .

Table 3. Vibrationally Averaged Rotational Constants \tilde{A} , \tilde{B} , and \tilde{C} for Selected Energy Levels^a

ν	\tilde{A}/cm^{-1}	\tilde{B}/cm^{-1}	\tilde{C}/cm^{-1}
0 ^P	0.432856	0.081456	0.072198
0 ^M	0.432856	0.081456	0.072198
5 ^P	0.485324	0.078591	0.070562
5 ^M	0.485324	0.078591	0.070562
10 ⁺	0.595842	0.074099	0.068206
10 ⁻	0.595842	0.074099	0.068206
11 ⁺	0.645901	0.072436	0.067369
11 ⁻	0.645896	0.072436	0.067369

^aFor localized parity states the difference in rotational constants between P- and M-species is $\lesssim 10^{-20} \text{ cm}^{-1}$.

Table 4. Centrifugal Distortion Constants of Fourth- and Sixth-Order Calculated *ab Initio* at the MP2/aug-cc-pVTZ Level at the Equilibrium Geometry of Cl–O–O–Cl

\tilde{D}_J	$6.4313 \times 10^{-8} \text{ cm}^{-1}$
\tilde{D}_{JK}	$-5.4271 \times 10^{-7} \text{ cm}^{-1}$
\tilde{D}_K	$3.9846 \times 10^{-6} \text{ cm}^{-1}$
\tilde{d}_1	$-1.7343 \times 10^{-8} \text{ cm}^{-1}$
\tilde{d}_2	$-8.0177 \times 10^{-10} \text{ cm}^{-1}$
\tilde{H}_J	$1.5653 \times 10^{-13} \text{ cm}^{-1}$
\tilde{H}_{JK}	$-1.0712 \times 10^{-12} \text{ cm}^{-1}$
\tilde{H}_{KJ}	$-1.2353 \times 10^{-11} \text{ cm}^{-1}$
\tilde{H}_K	$7.5386 \times 10^{-11} \text{ cm}^{-1}$
\tilde{h}_1	$8.3679 \times 10^{-14} \text{ cm}^{-1}$
\tilde{h}_2	$1.0189 \times 10^{-14} \text{ cm}^{-1}$
\tilde{h}_3	$-1.1485 \times 10^{-17} \text{ cm}^{-1}$

with $\hat{J}^2 = \hat{J}_x^2 + \hat{J}_y^2 + \hat{J}_z^2$ and $\hat{J}_\pm = \hat{J}_x \pm i\hat{J}_y$. The rotational constants A , B , and C were vibrationally averaged whereas constants for centrifugal distortion were approximated as the equilibrium values (Tables 3 and 4).

States including rotation are characterized by their angular momentum with additional quantum numbers $\mathbf{J} = J_{K_a K_c}$ in conventional notation.^{11,89} The changes of the tunneling splittings with rotational excitation were thus approximately

accounted for and fall in the range of 5% for low rotational excitations with $J < 5$. We neglected the influence of the parity violation on the moments of inertia, which is comparatively small but can be important for the calculation of rovibrational line shifts.^{48,91,92} A more detailed discussion of the procedure can be found in ref 68. We note that we have approximated here the, in principle, multidimensional matrix elements for parity violation (generated from a multidimensional parity violating potential⁹³) by the matrix element of the quadiabatic channel wave functions with a 1-dimensional parity violating potential. In this sense our approximation may be called quasiharmonic. Though multidimensional couplings can be important,⁹³ we can safely assume that they will not qualitatively change the basic effects studied here. The same is true for non Born–Oppenheimer effects. It has also been shown that nuclear spin effects can be important for the understanding of high-resolution spectra when parity violating effects are interpreted.⁹⁴ We neglect them at present, although they could be readily introduced as lower order effects.

2.2. Laser Interaction and Wavepacket Dynamics.

The third term in the Hamiltonian from eq 9 accounts for the interaction of the molecule with light. Here we investigate the interaction with a coherent, z -polarized monochromatic quasiclassical laser field with electric field strength $E_z \cos(\omega t + \eta)$,^{95–101} which is an excellent approximation for many conditions of typical laser excitation in the infrared, for example, where we set the phase $\eta = 0$. To solve the time-dependent Schrödinger equation, we introduce the time evolution operator $\hat{U}(t, t_0)$, which gives the general solution

$$\Psi(\mathbf{x}, t) = \hat{U}(t, t_0) \Psi(\mathbf{x}, t_0) \quad (17)$$

\hat{U} satisfies the equation:

$$i\hbar \frac{\partial \hat{U}(t, t_0)}{\partial t} = \hat{H}(\mathbf{x}, t) \hat{U}(t, t_0) \quad (18)$$

For simplicity we shall assume from now on that $t_0 = 0$. Using the basis set expansion from eq 5, we can write an equation for the time evolution operator in matrix form. In the spectroscopic basis this reads as

$$i \frac{dU_{jk}(t, 0)}{dt} = \left(2\pi c \tilde{\nu}_j \delta_{jk} - \frac{1}{\hbar} \langle \varphi_j | \mu_z | \varphi_k \rangle E_z(t) \cos(\omega t) \right) U_{jk}(t, 0) \quad (19)$$

with the electric dipole transition moments $\langle \varphi_j | \mu_z | \varphi_k \rangle$, which can be calculated from the stationary eigenstates φ_k . We solve eq 19 in the quasi resonant approximation (QRA^{68,95–100}), which allows us to separate the high-frequency oscillation of the electric field with frequency ω from the population transfer dynamics in case that

- the field is weak, i.e.

$$\frac{1}{\hbar} \langle \varphi_j | \mu_z | \varphi_k \rangle E_z(t) \ll \omega \quad (20)$$

which is the case for small field strengths,

- there are “quasiresonant” transitions, $j \leftarrow k$, for which

$$2\pi c |\tilde{\nu}_k - \tilde{\nu}_j| \ll \omega \quad (21)$$

In the QRA only transitions that are approximately separated by one quantum of laser irradiation are taken into account. The effective Hamiltonian in the QRA reads then

$$\mathbf{H}_{\text{QRA}}(t) = \mathbf{X} + \mathbf{V}_{\text{QRA}}(t) \quad (22)$$

where the quasi resonant basis is defined as

$$a_k(t) = \exp(in_k\omega t) b_k(t) \quad (23)$$

with the diagonal matrix of resonance defects relative to an integer n_k times the laser frequency

$$X_k = 2\pi c\tilde{\nu}_k - n_k\omega \quad (24)$$

and the coupling element in the quasisresonant approximation

$$(V_{\text{QRA}})_{kj}(t) = -\frac{1}{2\hbar} \langle \varphi_k | \mu_z | \varphi_j \rangle E_z(t) \quad (25)$$

$E_z(t)$ is the amplitude of the laser field and can be taken as slowly time-dependent.⁹⁸ For sufficiently small time intervals Δt the quasisresonant Hamiltonian stays constant,

$$\mathbf{H}_{\text{QRA}}(t+\Delta t) \approx \mathbf{H}_{\text{QRA}}(t) \quad (26)$$

The time evolution operator in the basis a_k can then be calculated stepwise as

$$\mathbf{U}^{(a)}(t+\Delta t, t) = \exp(-i[\mathbf{H}_{\text{QRA}}(t+\Delta t/2) \cdot \Delta t]) \quad (27)$$

The resonance defects are for now taken to be time-independent (constant laser frequency). However, in section 3.4 we will introduce frequency chirping of the laser. Important changes in the equations will be discussed there.

Knowing the matrix representation of the time evolution operator, \mathbf{U} , time-dependent populations can be obtained from the diagonal elements of \mathbf{U} . Time-dependent wavepackets can be represented as probability densities according to eq 28.

$$|\Psi(\mathbf{x}, t)|^2 = |\hat{U}(t, 0) \Psi(\mathbf{x}, 0)|^2 \quad (28)$$

3. STEREOMUTATION DYNAMICS OF Cl-O-O-Cl

In this section we report our results on several numerical simulations on the quantum dynamics under laser excitation in Cl-O-O-Cl. The molecule can be considered as a prototype molecule for axially chiral molecules where parity violation plays an important role for the dynamics. As we described in section 2.1, parity violation leads to the formation of a localized eigenstate in the ground state that represents a chiral geometry of the molecule. This localized state will act as the initial state for our simulations. In the following we will introduce several limiting cases of possible stereomutation dynamics in an axially chiral molecule under laser excitation. In section 3.1 we use a laser to prepare a superposition state that subsequently shows stereomutation dynamics. The stereomutation is due to the tunnel effect and is accordingly called “tunneling stereomutation” (TSM). This process was already discussed by Friedrich Hund.⁷ In section 3.2 we investigate a case where the stereomutation dynamics is due to population transfer during laser irradiation and may thus be called “laser-induced stereomutation” (LISM). What follows in section 3.3 is a special case of LISM that, considering the wavepacket dynamics, looks like TSM in the ground state but is in fact mediated by the laser. Because of the similarity to resonance Raman scattering, we call this process “resonance Raman induced stereomutation” (RRISM).

Section 3.4 discusses the effect of modulating the frequency of a laser pulse, which finds an application in section 3.5 where we show simulations of an experiment to measure the parity violating energy difference between enantiomers of a chiral molecule. Cl-O-O-Cl is discussed as a realistic prototype molecule and thus our simulation serves as (theoretical) proof of principle for such an experiment.

For all experiments we used a Gaussian intensity distribution of the laser pulse, i.e.^{98,99}

$$I(t) = I_{\text{max}} \exp(-2(t - t_0)^2 / \tau_p^2) \quad (29)$$

the characteristic parameters are thus the laser frequency $\nu_L = c\tilde{\nu}_L$, the maximum intensity I_{max} and the pulse length τ_p . All results are reported with only the ground state being populated initially ($T = 0$ K).

3.1. Tunneling Stereomutation after Coherent Excitation. The basic excitation scheme used for this simulation can be seen in Figure 5. We start with a chiral state,

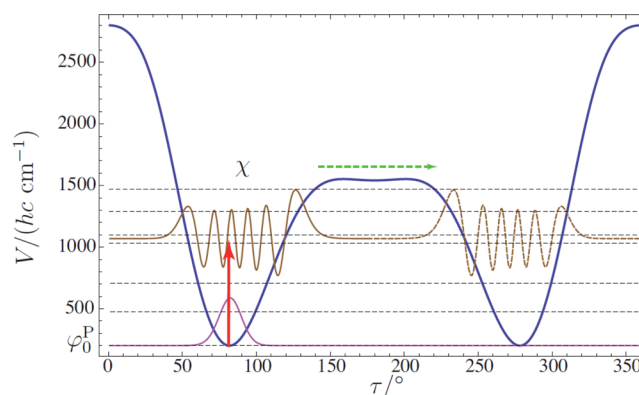


Figure 5. Excitation scheme: Starting with a chiral ground state, a chiral state χ ($\nu = 10$) near the barrier is populated after laser irradiation. After the excitation of χ , one expects tunneling stereomutation (TSM) during field-free evolution, because χ is a superposition of two parity eigenstates.

φ_0^P (eq 14). With a sufficiently intense laser pulse we excite to another, initially chiral state lying close to 1000 cm^{-1} (Figure 5) where the tunneling splitting is already much larger than parity violation ($\nu = 10$). Therefore, tunneling switching^{62,64} occurs, and the excited chiral state is not an eigenstate of the molecular system but a superposition of achiral parity eigenstates, which is expected to show tunneling stereomutation during the field-free evolution time.

The time dependent chiral state obtained after excitation can be written as follows (for simplicity we omit the overall phase):

$$\chi(t=0) = \frac{1}{\sqrt{2}}(\varphi_{10}^+ + \varphi_{10}^-) \quad (30)$$

the time $t = 0$ indicates the beginning of the field-free evolution. In Table 5 the energies of the states used in this simulation are listed on the diagonal in terms of their wavenumber values.

Hund showed that such a superposition of parity eigenstates will change its chirality periodically with a full period dependent on the tunneling splitting:⁷

$$\tau_{\text{TSM}} = h/(\Delta E) = 1/(c\Delta\tilde{\nu}) \quad (31)$$

For efficient excitation the laser was chosen to be on-resonance with the transition from φ_0^P to χ . The parameters

Table 5. Dipole Transition Moments of Rovibrational States in Debye Given as Off-Diagonal Elements^a

$\hat{\mu}$	$ 0^P, 0_{0,0}\rangle$	$ 0^M, 0_{0,0}\rangle$	$ 10^+, 1_{1,1}\rangle$	$ 10^-, 1_{1,1}\rangle$
$\langle 0_{0,0}, 0^P $	0			
$\langle 0_{0,0}, 0^M $	0	5.8×10^{-13}		
$\langle 1_{1,1}, 10^+ $	-1.54×10^{-6}	-1.54×10^{-6}	1104.25864746	
$\langle 1_{1,1}, 10^- $	-1.54×10^{-6}	1.54×10^{-6}	0.71	1104.25864748

^aOn the diagonal, the eigenstate energies are given as $E/(hc)$ in units of cm^{-1} . The notation follows eq 13, where the elevated index denotes the limiting cases of localized (P/M) or delocalized (\pm) eigenstates with torsional quantum number ν . $J_{K_a K_c}$ are the rotational quantum numbers. States with low torsional quantum number ($\nu = 0$) are chiral states separated by the parity violating energy difference $\Delta_{\text{pv}} E_0$. Excited torsional states ($\nu = 10$) are states of well-defined parity. Note that the tunneling splitting is much smaller than the power broadening (Table 6) such that both states will be excited simultaneously by the laser.

Table 6. Excitation Wavenumber $\tilde{\nu}_L$, Maximum Intensity I_{max} , Power Broadening $\Delta\tilde{\nu}_{\text{pb}}$, and Pulse Length τ_p of the Laser^a

$$\begin{aligned}\tilde{\nu}_L &= 1104.2586 \text{ cm}^{-1} \text{ (resonant)} \\ I_{\text{max}} &= 30 \text{ MW cm}^{-2} \\ \Delta\tilde{\nu}_{\text{pb}} &= 3.9 \times 10^{-6} \text{ cm}^{-1} \\ \tau_p &= 5 \mu\text{s}\end{aligned}$$

^aThe power broadening is much larger than the tunneling splitting of the excited state at $\nu = 10$ (Table 5); therefore, both tunneling components will be excited during laser irradiation.

chosen for the laser field are shown in Table 6, and the dipole transition moments for rovibrational transitions are collected in Table 5. The “power broadening” of the pulse connecting the states j and k is calculated approximately¹⁰¹ as twice the coupling element V_{QRA} from eq 25 but given in units of cm^{-1} :

$$\Delta\tilde{\nu}_{\text{pb}}/\text{cm}^{-1} = 2 \times 0.461 \left| \frac{\langle \varphi_j | \mu_z | \varphi_k \rangle}{\text{Debye}} \right| \sqrt{I/\text{MW cm}^{-2}} \quad (32)$$

The rovibrational selection rules are (b -type transitions with $J = 0 \leftarrow J = 0$ forbidden):

$$\begin{aligned}\Delta J &= 0, \pm 1, \quad \Delta K_a = \pm 1, \pm 3, \pm 5, \dots \\ \Delta K_c &= \pm 1, \pm 3, \pm 5, \dots\end{aligned} \quad (33)$$

The relevant energies and power broadening conditions are such that only one tunneling doublet is excited. The time-dependent population during laser excitation can be seen in Figure 6.

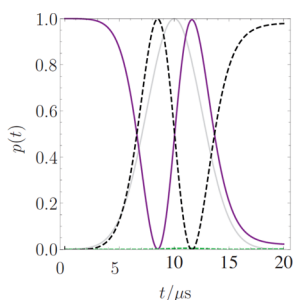


Figure 6. Time-dependent populations of ground state φ_0^P (full line) and the excited state χ (dashed) during laser interaction (Gaussian pulse shape shown in addition and normalized to maximum relative intensity). Almost total population transfer from φ_0^P to χ is observed at appropriate times.

During the irradiation the population oscillates between φ_0^P and χ as does the average energy of the quantum state. The wavepacket in Figure 7 illustrates this process at initial times $t \leq 15 \mu\text{s}$.

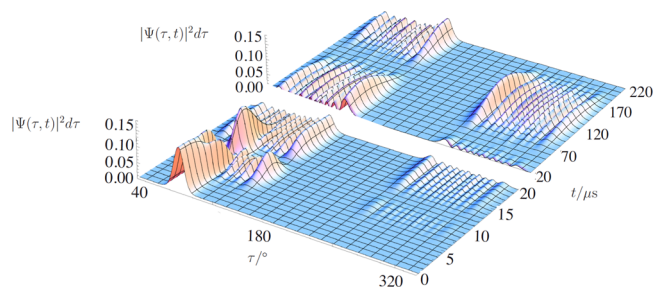


Figure 7. Time-dependent wavepacket for $0 \leq t \leq 220 \mu\text{s}$ with $d\tau = \Delta\tau = 1^\circ$. Early times: Wavepacket during excitation. After about $15 \mu\text{s}$, the laser field is off and field-free evolution starts, which will eventually lead to tunneling stereomutation (TSM) of the chiral state χ . Later times: Wavepacket showing TSM during field-free evolution of the molecular state. The period is roughly $200 \mu\text{s}$, in accordance with eq 31.

The tunneling stereomutation already sets in. However, the tunneling period is about 1 order of magnitude larger than the pulse length, which means that the stereomutation will be fully visible only for longer times after the excitation process has finished (Figure 7, $t > 15 \mu\text{s}$). In this case the excitation process and the stereomutation process can be separated: first preparation of a chiral superposition state, then stereomutation due to TSM under field-free conditions.

3.2. Laser-Induced Stereomutation. Here, the excited state lies one quantum of torsional excitation higher than in section 3.1, at about 1200 cm^{-1} ($\nu = 11$). Consequently, the tunneling splitting will be 1–2 orders of magnitude larger than before. Using a laser with similar power broadening as described in section 3.1, we are now able to selectively excite one parity eigenstate. Each parity eigenstate is, however, also coupled to chiral states of both the P- and the M-enantiomeric species. One could thus in principle excite from φ_0^P to the intermediate state φ_{11}^+ with a first laser pulse and then use a second laser pulse to transfer the population to the chiral state φ_0^M . One would have then realized a stereomutation process by transferring the population from one chiral state to another via an intermediate parity eigenstate. Instead, we choose the laser pulse length large enough such that the same laser works as pump and transfer pulse (the laser approximates, therefore, the continuous wave limit). This is possible because the chiral states φ_0^P and φ_0^M are only separated by a tiny splitting, namely $\Delta_{\text{pv}} E$, and are approximately degenerate, such that the laser pulse is in resonance with both the transition $\varphi_{11}^+ \leftarrow \varphi_0^P$ and $\varphi_0^M \leftarrow \varphi_{11}^+$. See Figure 8 for the excitation scheme; energies and field parameters can be found in Tables 7 and 8.

The tunneling splitting is itself not relevant for the time scale of the stereomutation. The relevant parameter is the coupling

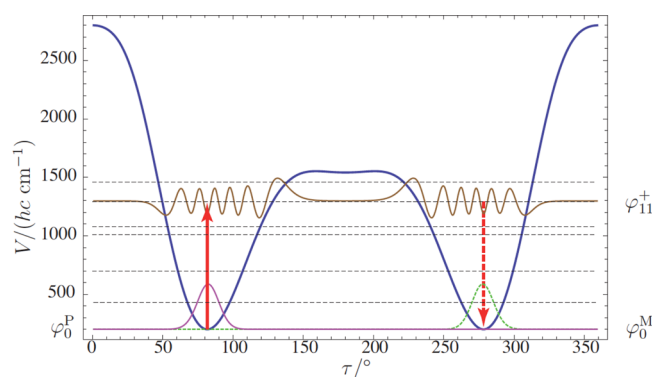


Figure 8. Excitation scheme: Starting with the chiral ground state φ_0^P , a parity eigenstate near the barrier, φ_{11}^+ , is populated with a long laser pulse of low intensity. Therefore, the same laser pulse depopulates the state again, eventually leading to the population of another chiral state, φ_0^M , lying on the other side of the potential barrier.

strength which depends on the intensity of the laser pulse. Therefore, one might call this kind of dynamics “laser-induced stereomutation” (LISM). Time-dependent populations are shown in Figure 9. After the excitation process, the parity eigenstate φ_{11}^+ is hardly populated. The population is almost completely transferred to the M-enantiomer.

To keep track of the “chirality” of the wavepacket, we integrate the time-dependent wavepacket over one-half of the space,^{102,103} i.e.

$$p_\chi(t) = \int_{\Lambda_\chi} |\Psi(\tau, t)|^2 d\tau \quad (34)$$

with $\Lambda_P = \{\tau \in \mathbb{R} | \tau < 180^\circ\}$ (“P-enantiomeric species”) and $\Lambda_M = \{\tau \in \mathbb{R} | \tau > 180^\circ\}$ (“M-enantiomeric species”). The time-dependent chirality $p_\chi(t)$ is shown in Figure 10, the time-dependent wavepacket is shown in Figure 11 and illustrates the occurrence of LISM.

3.3. Resonance Raman Induced Stereomutation. Now, we change the laser parameters to introduce a small resonance defect Δ_L . To ensure an efficient population transfer, we scale the intensity and duration of our pulse accordingly (Table 9). The relevant states and transition moments are the same as in section 3.2 (Table 7). This implies that couplings to further rovibrational states are not important for the dynamics.

This process bears some similarity to Raman scattering and is a limiting case of LISM, where the laser is so much off-resonance to the transition from the P-enantiomer to the intermediate state that the population is “immediately” transferred to the M-enantiomer without important remaining population in the excited states (Figure 12). Assuming that only one

Table 8. Excitation Wavenumber $\tilde{\nu}_L$, Maximum Intensity I_{\max} , Power Broadening $\Delta\tilde{\nu}_{pb}$, and Pulse Length τ_p of the Lasers^a

$$\begin{aligned} \tilde{\nu}_L &= 1186.7912 \text{ cm}^{-1} \text{ (resonant)} \\ I_{\max} &= 3.4 \text{ GW cm}^{-2} \\ \Delta\tilde{\nu}_{pb} &= 7.5 \times 10^{-6} \text{ cm}^{-1} \\ \tau_p &= 5 \mu\text{s} \end{aligned}$$

^aThe power broadening is now smaller than the tunneling splitting of the excited state (compare with Table 7); therefore, one can selectively excite one parity eigenstate.

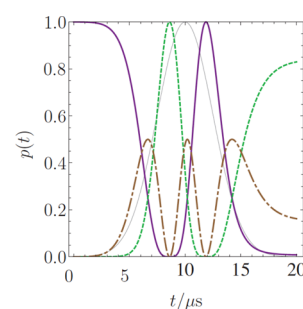


Figure 9. Time-dependent populations of states φ_0^P (full line), φ_0^M (dashed), and φ_{11}^+ (dash-dotted) during laser excitation. The Gaussian pulse shape is shown in addition and normalized to maximum relative intensity.

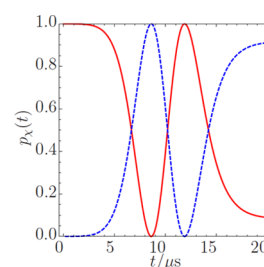


Figure 10. Time-dependent “chirality” from eq 34 clearly showing the process of LISM (P-species, full line; M-species, dashed).

near-resonant level is effective in mediating this process, one might call it “resonance Raman induced stereomutation” (RRISM).

From looking at the time-dependent wavepacket (Figure 13) only, one would assume that this is an example of TSM in the ground state. However, in our case the chiral states are stable under field-free conditions due to the comparatively large parity violation ($\Delta_{pv}E \gg \Delta\tilde{\nu}_0$). The stereomutation is due to population transfer between the two chiral states and not due to tunneling motion. Even if $\Delta_{pv}E$ were completely vanishing,

Table 7. Dipole Transition Moments of Rovibrational States in Debye Given as Off-Diagonal Elements^a

$\hat{\mu}$	$ 0^P, 0_{0,0}\rangle$	$ 0^M, 0_{0,0}\rangle$	$ 11^+, 1_{1,1}\rangle$	$ 11^-, 1_{1,1}\rangle$
$\langle 0_{0,0}, 0^P $	0			
$\langle 0_{0,0}, 0^M $	0	5.8×10^{-13}		
$\langle 1_{1,1}, 11^+ $	-2.82×10^{-7}	-2.82×10^{-7}	1186.79115777	
$\langle 1_{1,1}, 11^- $	-2.82×10^{-7}	2.82×10^{-7}	0.69	1186.79127393

^aOn the diagonal, the eigenstate energies are given as $E/(hc)$ in units of cm^{-1} . The notation follows eq 13, where the elevated index denotes the limiting cases of localized (P/M) or delocalized (\pm) eigenstates with torsional quantum number ν . $J_{K_w K_c}$ is the rotational quantum number. States with low torsional quantum number ($\nu = 0$) are chiral states separated by the parity violating energy difference $\Delta_{pv}E_0$. Excited torsional states ($\nu = 11$) are states of well-defined parity.

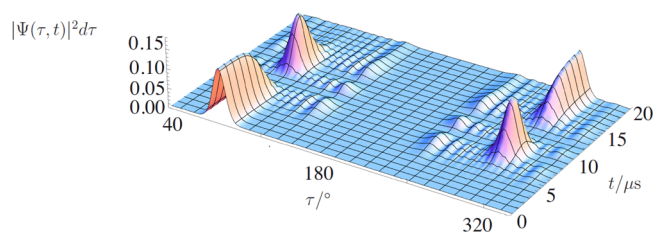


Figure 11. Time-dependent wavepacket during the excitation showing LISM while coupling two chiral states via an intermediate achiral state (see also Figure 9). The wavepacket is shown for $0 \leq t \leq 20 \mu\text{s}$ with $d\tau = \Delta\tau = 1^\circ$.

Table 9. Excitation Wavenumber $\tilde{\nu}_L$, Resonance Defect Δ_L , Maximum Intensity I_{max} , Power Broadening $\Delta\tilde{\nu}_{\text{pb}}$, and Pulse Duration τ_p of the Laser

$$\begin{aligned}\tilde{\nu}_L &= 1186.791 \text{ cm}^{-1} \\ \Delta_L &\approx 2 \times 10^{-4} \text{ cm}^{-1} \\ I_{\text{max}} &= 70 \text{ GW cm}^{-2} \\ \Delta\tilde{\nu}_{\text{pb}} &= 3.5 \times 10^{-5} \text{ cm}^{-1} \\ \tau_p &= 25 \mu\text{s}\end{aligned}$$

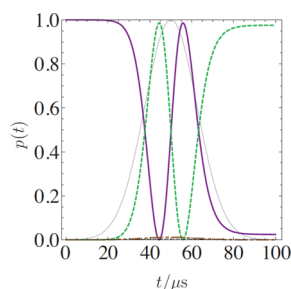


Figure 12. Time-dependent populations of states ϕ_0^{P} (full line), ϕ_0^{M} (dashed), and ϕ_{11}^{M} (dashed-dotted) during laser excitation (Gaussian pulse shape shown in addition and normalized to maximum relative intensity). The intermediate state ϕ_{11}^{M} is off-resonance, leading to immediate population transferred to state ϕ_0^{M} .

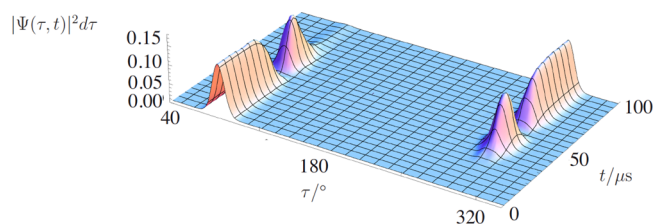


Figure 13. Time-dependent wavepacket during excitation. The adiabatic population transfer leads to a stereomutation process in the torsional ground state. Because of its similarity to the Raman scattering processes, it can be called resonance Raman induced stereomutation (RRISM). The wavepacket is shown for $0 \leq t \leq 100 \mu\text{s}$ with $d\tau = \Delta\tau = 1^\circ$.

the result would not be dependent on the tunneling splitting, because the period of TSM would be orders of magnitude larger than for RRISM due to the small tunneling splitting in the ground state.

3.4. Frequency-Modulated Pulses. In this section we investigate the use of frequency-modulated pulses for such experiments with chiral molecules. The results presented here are related to earlier work using chirped pulses used for adiabatic population transfer^{104–106} as well as to ongoing experimental work in our group.^{107–109} As we have discussed in

section 3.2, depending on pulse duration and coupling strength (intensity), the population can oscillate between various states, even more so if we investigate nonzero temperature cases where frequency-modulated pulses might also be applied.⁶⁸ If we want to selectively excite one single quantum state, we have to adjust several parameters of the laser field to guarantee an optimal population transfer. We could, for example, reduce the pulse duration such that we end up in a quantum state where the population transfer is maximized. We could adjust the intensity or use only resonant pulses to have a more efficient population transfer and to adjust the period of Rabi oscillations accordingly. Even if the population transfer is maximized at the end of the pulse, we might find that the population oscillates several times between initial and final state.

Alternatively, we can arrive at a stable population inversion that is not too sensitive to small variations of these external parameters, by introducing the modulation of the laser frequency leading to a so-called “chirped” pulse. To demonstrate the effect of chirping, we look at an excitation similar to those studied in sections 3.1–3.3. The basic scheme can be seen in Figure 14; see also Table 7 for the molecular parameters.

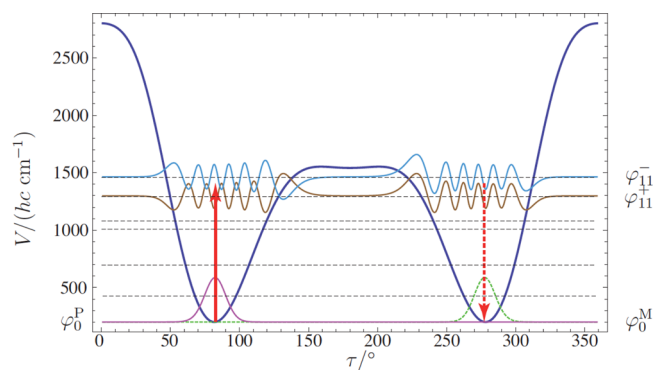


Figure 14. Excitation scheme: Starting with the chiral ground state ϕ_0^{P} , both parity eigenstates near the barrier, ϕ_{11}^{P} and ϕ_{11}^{M} , are populated using a sufficiently intense laser pulse with linearly modulated frequency. With the same laser pulse, the states are then depopulated toward the two chiral states ϕ_0^{P} and ϕ_0^{M} .

This scheme is similar to what has been discussed in section 3.2; however, both parity eigenstates will play a role depending on the frequency modulation. The limiting cases of zero, weak or strong frequency modulation are investigated.

We excite from the initial state, ϕ_0^{P} , to both parity eigenstates near the barrier, which are also coupled to the other enantiomeric species ϕ_0^{M} . Table 10 gives an overview of the

Table 10. Excitation Wavenumber $\tilde{\nu}_L$, Maximum Intensity I_{max} , Power Broadening $\Delta\tilde{\nu}_{\text{pb}}$, Pulse Length τ_p , and the Different Modulation Strengths δ_ν of the Laser

$$\begin{aligned}\tilde{\nu}_L &= 1186.7912 \text{ cm}^{-1} \text{ (resonant)} \\ I_{\text{max}} &= 27 \text{ GW cm}^{-2} \\ \Delta\tilde{\nu}_{\text{pb}} &= 2.1 \times 10^{-5} \text{ cm}^{-1} \\ \tau_p &= 5 \mu\text{s} \\ \delta_\nu &= 0 \text{ MHz}/\mu\text{s}, +0.04 \text{ MHz}/\mu\text{s}, -1.4 \text{ MHz}/\mu\text{s}\end{aligned}$$

laser parameters used here. We assume that without frequency modulation the power broadening of the laser pulse is smaller than the tunneling splitting between states ϕ_{11}^{P} and ϕ_{11}^{M} .

The intensity was chosen such that we observe several oscillations in population transfer during one pulse (compare the time-dependent population in Figure 15 with the results in

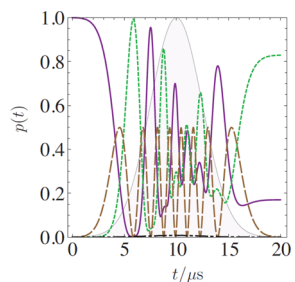


Figure 15. Time-dependent populations of states φ_0^P (full line), φ_0^M (dashed), and φ_{11}^+ (large dashes) during excitation (Gaussian pulse shape shown in addition and normalized to maximum relative intensity) without frequency modulation. The population of state φ_{11}^- (dashed-dotted) is very small and thus hardly visible. After excitation, the state φ_{11}^+ is not populated.

Figure 9 from section 3.2). Similarly, the time-dependent wavepacket in Figure 16 shows LISM with the population of a chiral state after the excitation process.

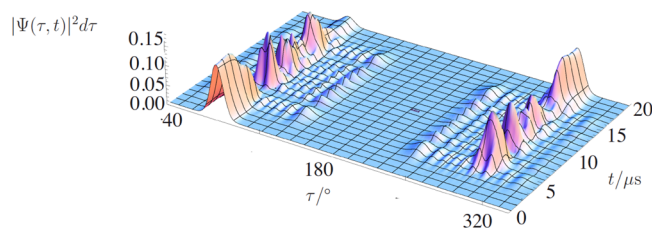


Figure 16. Time-dependent wavepacket during laser excitation without frequency modulation. LISM with final population of a chiral state of opposite enantiomeric structure. The wavepacket is shown for $0 \leq t \leq 20 \mu\text{s}$ with $d\tau = \Delta\tau = 1^\circ$.

We introduce frequency modulation of the laser by linearly changing the laser frequency around a center frequency ω_0 such that ω_0 is reached at the point of maximum intensity of the pulse. Let the time-dependent laser frequency be written as

$$\omega(t) = \omega_0 - 2\pi\delta_\nu t \quad (35)$$

with the frequency modulation $|2\pi\delta_\nu t| \ll \omega_0, \forall t$ during the pulse. If we introduce $\omega(t)$ in the equations from section 2.2, the resonance defect from eq 24 in the quasi resonant approximation transforms to

$$X'_k = X_k + 4\pi\delta_\nu t \quad (36)$$

and thus becomes time-dependent. Note that the initial frequency modulation of $2\pi\delta_\nu t$ becomes a resonance defect of $4\pi\delta_\nu$ in the QRA. The discretization step Δt has to be chosen such as to guarantee eq 26 to hold.

If we introduce a weak modulation, we are now able to selectively maximize the population transfer from the ground state φ_0^P to the excited state φ_{11}^+ . The time-dependent populations are shown in Figure 17, and the time-dependent wavepacket is shown in Figure 18. We first note that we see LISM, similar to the time-dependent wavepacket shown in Figure 16, but the dynamics is more regular and, more importantly, the final state is an achiral state, which is in accordance with the fact that we populated φ_{11}^+ . Further calculations

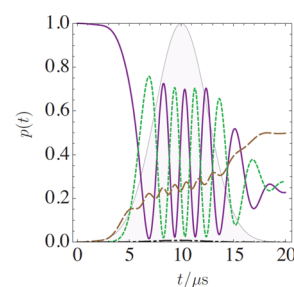


Figure 17. Time-dependent populations of states φ_0^P (full line), φ_0^M (dashed), and φ_{11}^+ (large dashes) during excitation (Gaussian pulse shape shown in addition and normalized to maximum relative intensity) with small frequency modulation. The population of state φ_{11}^- (dashed-dotted) is hardly visible. After excitation, the state φ_{11}^+ is populated with $p_{\varphi_{11}^+} \approx 0.5$.

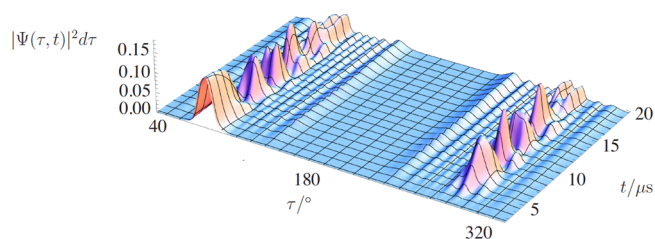


Figure 18. Time-dependent wavepacket during laser excitation with small frequency modulation. Again LISM, but with final population of an excited achiral state. The wavepacket is shown for $0 \leq t \leq 20 \mu\text{s}$ with $d\tau = \Delta\tau = 1^\circ$.

showed that this result is stable under slight variation of the modulation strength.

We also investigate the effect of strong frequency modulation. In this case the modulation strength is chosen such that it is of the same order of magnitude as the tunneling splitting between φ_{11}^+ and φ_{11}^- . Therefore, we expect to excite both parity eigenstates, which is confirmed in Figure 19, showing the

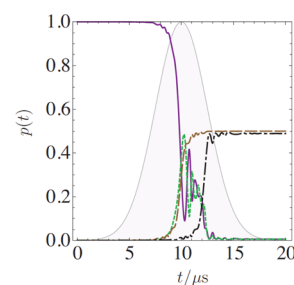


Figure 19. Time-dependent populations of states φ_0^P (full line), φ_0^M (dashed), φ_{11}^+ (long dashes), and φ_{11}^- (dashed-dotted) during excitation (Gaussian pulse shape shown in addition and normalized to maximum relative intensity) with high-frequency modulation. After excitation, only a superposition of parity eigenstates φ_{11}^+ and φ_{11}^- is populated.

time-dependent populations. The delay in populating these states can be controlled by adjusting the strength and sign of δ_ν . The time-dependent wavepacket in Figure 20 (early times) suggests that we populate a superposition of φ_{11}^+ and φ_{11}^- and thus a chiral state. As in section 3.1, we expect TSM under field-free conditions for this state, which is shown in Figure 20 (later times). The period depends on the tunneling splitting and is $\tau_{\text{TSM}} \approx 0.3 \mu\text{s}$, which is in agreement with eq 31.

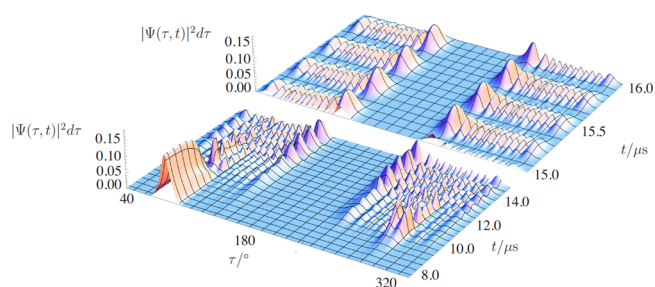


Figure 20. Time-dependent wavepacket during laser excitation with high-frequency modulation with $d\tau = \Delta\tau = 1^\circ$. Early times: LISM for the first 12 μs , with final population of a chiral state that is a superposition of two parity eigenstates, then TSM. Later times: Enlargement to show TSM under field-free conditions. The period $\tau_{\text{TSM}} \approx 0.3 \mu\text{s}$.

Again, this result is stable under slight variation of the modulation strength.

Thus, we have shown here how one could enforce the limiting cases of stereomutation by adjusting the modulation strength of the laser. Compared to optimizing several parameters like pulse duration, intensity, or resonance condition, this has the advantage that one has to basically adjust only one parameter. Furthermore, the overall behavior of the population transfer is less sensitive to the exact values of the modulation frequency as long as we stay in the limiting cases of weak or strong modulation, respectively. If we have more than one target state, we can also adjust the delay due to different resonance defects or transition strengths with the help of this parameter. Experimentally, the linear modulation of laser frequency could also be realized by quadratically modulating the phase.

We finally want to use the results from the previous sections to simulate an experiment that uses a time-resolved measurement scheme to determine the parity violating energy difference in a chiral molecule^{8,12,54} for the realistic case of Cl–O–O–Cl.

3.5. Time Evolution of Molecular Parity Due to Electroweak Parity Violation. 3.5.1. General Information.

Using the results from the previous sections, we are able to simulate a possible measurement of molecular parity violation for a realistic case. The experimental scheme was already proposed in earlier publications^{8,12,54,62,65} and shall be summarized in the following. The experiment is based on a time-resolved measurement scheme where a molecular superposition of chiral states that has almost perfectly defined parity must be prepared

in the first step. To achieve this, one has to excite a suitable intermediate excited eigenstate of well-defined parity with a first laser pulse, which is followed by the transfer of the state's population to a superposition of chiral states forming a state of initially well-defined parity which is, however, time-dependent because of electroweak parity violation. From recording this time dependence, e.g., by a third probe laser, one can extract the energy difference separating the two chiral states forming the superposition state, i.e., the parity violating energy difference $\Delta_{\text{pv}}E$. Although such an experiment seems much harder to do than frequency-resolved measurements of spectral lines, there are several advantages of the time evolution experiment:

- First, one need not resolve $\Delta_{\text{pv}}E$ directly by high-resolution measurements. $\Delta_{\text{pv}}E/h$ lies, in our case, on the order of several millihertz ($\sim 10^{-12} \text{ cm}^{-1}$) which is too small to be resolved spectroscopically to date. In fact, in the time-resolved experiment proposed here one has to achieve the single population of a rovibrational quantum state, which needs, in the case of Cl–O–O–Cl, a relative resolution $\Delta\nu/\nu$ of ca. 10^{-7} at roughly 1000 cm^{-1} , which can readily be achieved today corresponding to resolutions in the megahertz and sub-megahertz range.^{108,109}
- Second, the experiment can be done for resolved enantiomers as well as racemic mixtures, which makes an enantioselective synthesis or a separation of enantiomers unnecessary. Indeed, one can say that the idea of the experiment is to prepare *in situ* (in a molecular beam) a well-defined “parity isomer” at $t = 0$.⁵⁴

To start with the preparation, we have to identify a suitable intermediate state. Any state with well-defined parity is, in principle, suitable. In Cl–O–O–Cl we can make use of the effect of tunneling switching: For highly excited states near the stereomutation barrier, the tunneling splitting becomes dominant ($hc\Delta\tilde{\nu}_{\pm} \gg \Delta_{\text{pv}}E$) and the molecular eigenstates are states of well-defined parity opposed to the localized ground and low-lying excited states. Furthermore, we want to excite a single rovibrational quantum state, so we have to make sure that no other state lies within the width of the laser. We choose the laser such that it can discriminate between states separated by 10^{-4} cm^{-1} or more. The state we use as intermediate state is labeled φ_{11}^+ (Table 11). When transferring the population from the state of well-defined parity to a superposition of chiral states, we choose two chiral states other than the ground state, labeled φ_S^P and φ_S^M , respectively (Table 11). The parity

Table 11. Electric Dipole Transition Moments of Rovibrational States in Debye^a

μ	$ 0^P, 0_{0,0}\rangle$	$ 0^M, 0_{0,0}\rangle$	$ S^P, 0_{0,0}\rangle$	$ S^M, 0_{0,0}\rangle$	$ 11^+, 1_{1,1}\rangle$	$ 11^-, 1_{1,1}\rangle$
$\langle 0_{0,0}, 0^P $	0					
$\langle 0_{0,0}, 0^M $	0	5.8×10^{-13}				
$\langle 0_{0,0}, S^P $	0^a	0^a	593.82516943			
$\langle 0_{0,0}, S^M $	0^a	0^a	0	$593.82516943 + 5.5 \times 10^{-13}$		
$\langle 1_{1,1}, 11^+ $	-2.82×10^{-7}	-2.82×10^{-7}	-4.94×10^{-6}	-4.94×10^{-6}	1186.79115777	
$\langle 1_{1,1}, 11^- $	-2.82×10^{-7}	2.82×10^{-7}	-4.94×10^{-6}	4.94×10^{-6}	0.69	1186.79127393

^a0 due to selection rules for rovibrational transition. ^aDipole transition moments of rovibrational states in Debye given as off-diagonal elements. On the diagonal, the eigenstate energies are given as $E/(hc)$ in units of cm^{-1} . The notation follows eq 13, where the elevated index denotes the limiting cases of localized (P/M) or delocalized (\pm) eigenstates with torsional quantum number ν . $J_{K_v K_c}$ is the rotational quantum number. States with low torsional quantum number ($\nu = 0-5$) are chiral states separated by the parity violating energy difference $\Delta_{\text{pv}}E_0$. Excited torsional states ($\nu = 11$) are states of well-defined parity.

eigenstate has to be in a rotationally excited state ($J_{K_a K_b} = 1_{1,1}$) due to the rovibrational selection rules in eq 33.

3.5.2. *Preparing a Superposition of Chiral Enantiomers with Well-Defined Parity.* In Figure 21 we show the excitation

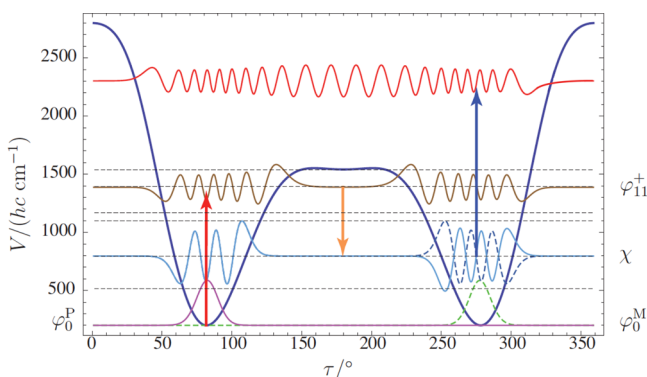


Figure 21. Preparation: Excitation of φ_{11}^+ using a frequency-modulated pulse (left arrow, pump) and population transfer to a superposition χ formed by the two chiral eigenstates φ_5^P and φ_5^M (middle arrow, transfer). Detection: Time-dependent parity of χ is recorded for different times of field-free evolution after preparation by a third pulse (right arrow, probe). $\Delta_{pv}E$ can then be extracted.

scheme with three laser pulses: With the first pulse we excite from the ground state, φ_0^P ($0_{0,0}$), to the state of well-defined parity φ_{11}^+ ($1_{1,1}$). The second pulse transfers the population from φ_{11}^+ to a superposition state χ formed by two chiral states, φ_5^P and φ_5^M (both $0_{0,0}$). Due to dipole selection rules the initial parity of χ has to be negative. However, χ is not an eigenstate of the molecular system; therefore, it evolves under field-free conditions and changes its parity. With a third laser pulse this change in parity can be observed by recording the intensity of the transition from χ to a high-lying state of well-defined parity after different times of field-free evolution after the preparation. In an actual experimental setup this excited state is detected with very high sensitivity by REMPI (resonantly enhanced multiphoton ionization).^{108–110} To achieve efficient population transfer, we use frequency-modulated pulses as introduced in section 3.4. It is crucial to keep the intensity of the laser small enough (in our case roughly below several 100 GWcm⁻²) so that the state φ_{11}^- with negative parity is not populated. Also, the modulation strength must be kept low enough (below 1 MHz/ μ s) to ensure that population of φ_{11}^- is avoided.

Table 11 gives an overview over the dipole transition moments used, and in Table 12 the parameters chosen for pump and transfer pulses are shown. The laser width is limited by the natural line width and power broadening. Doppler broadening is smaller than the assumed laser width of 10^{-4} cm⁻¹ and can be neglected for very low temperatures in an appropriate molecular beam set up.^{108,109}

The time-dependent populations during the pump excitation are shown in Figure 22. Due to the small frequency modulation, the state φ_{11}^+ of positive parity is populated whereas the state φ_{11}^- of negative parity is hardly excited ($p \approx 10^{-10}$). The time-dependent wavepacket is shown in Figure 23. One sees how the chiral ground state is excited to a state that is spread across large parts of the total torsional range. The population dynamics during the transfer pulse are shown in Figure 24 with the corresponding time-dependent wavepacket in Figure 25.

3.5.3. *Detecting the Time-Dependent Parity.* After the preparation stage, half of the total population is in the

Table 12. Wavenumber $\tilde{\nu}_l$ of the Laser, Max Intensity I_{\max} , Power Broadening $\Delta\tilde{\nu}_{pb}$, and Pulse Duration τ_p for Pump and Transfer Pulse^a

$\tilde{\nu}_l^{\text{pump}} = 1186.7912$ cm ⁻¹ (resonant)
$I_{\max}^{\text{pump}} = 0.5$ GW cm ⁻²
$\Delta\tilde{\nu}_{pb}^{\text{pump}} = 3.1 \times 10^{-6}$ cm ⁻¹
$\tau_p^{\text{pump}} = 5$ μ s
$\tilde{\nu}_l^{\text{transfer}} = 593.8252$ cm ⁻¹ (resonant)
$I_{\max}^{\text{transfer}} = 1.6$ MW cm ⁻²
$\Delta\tilde{\nu}_{pb}^{\text{transfer}} = 2 \times 10^{-6}$ cm ⁻¹
$\tau_p^{\text{transfer}} = 5$ μ s
$\delta_\nu = 40$ kHz/ μ s

^aThe frequency modulation δ_ν was chosen to be equal for both pulses.

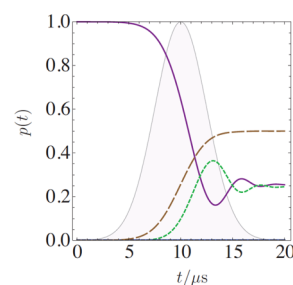


Figure 22. Time-dependent populations of states φ_0^P (full line), φ_0^M (dotted), and φ_{11}^+ (large dashes) during excitation with a Gaussian laser pulse (shown in addition and normalized to maximum relative intensity). The frequency is modulated to ensure efficient population transfer. φ_{11}^- is not populated significantly after excitation ($p \approx 10^{-10}$).

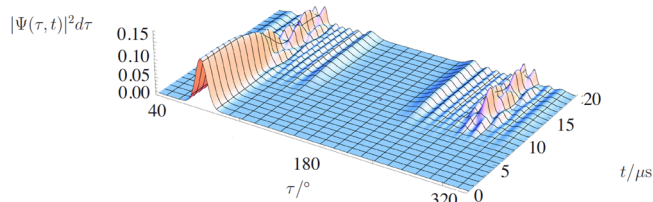


Figure 23. Time-dependent wavepacket during the pump process shown for $0 \leq t \leq 20$ μ s with $d\tau = \Delta\tau = 1^\circ$. The chiral ground state is excited to an achiral intermediate state, which is delocalized in space and has a well-defined parity.

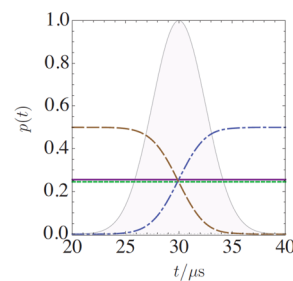


Figure 24. Time-dependent populations of states φ_0^P (full line), φ_0^M (dotted), and φ_{11}^+ (large dashes) during transfer to a superposition state χ (dash-dotted) with a Gaussian laser pulse (shown in addition and normalized to maximum relative intensity). The frequency is modulated to ensure efficient population transfer.

superposition χ of chiral states φ_5^P and φ_5^M . The remainder of the total population is still in the initial chiral ground state enantiomers, which can be considered “inert” for the remaining experiment. However, one has to account for a loss of intensity

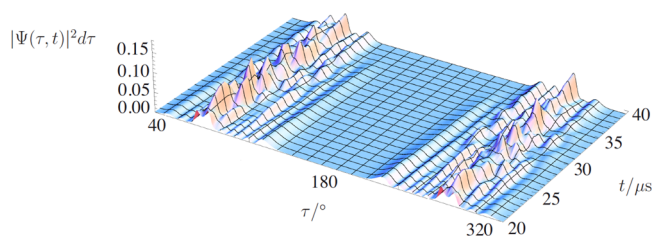


Figure 25. Time-dependent wavepacket during the transfer process shown for $0 \leq t \leq 20 \mu\text{s}$ with $d\tau = \Delta\tau = 1^\circ$. The delocalized wavepacket generated after the pump pulse becomes a wavepacket of a superposition state χ with initially well-defined parity (at $t \approx 40 \mu\text{s}$) after using a frequency-modulated transfer pulse. At much longer times ($t > 1 \text{ ms}$); however, the parity is time-dependent leading to nonzero detection probability (Figure 26).

during the detection step. Under field-free conditions the superposition χ shows a time evolution. Omitting an overall phase, χ can be written at the beginning of this field-free evolution (written at a new time zero ($t = 0$) corresponding to $40 \mu\text{s}$ in Figure 25) as

$$\chi(t=0) = \frac{1}{\sqrt{2}}(\varphi_5^{\text{P}} - \varphi_5^{\text{M}}) \stackrel{\text{def}}{=} \varphi_5^- \quad (37)$$

At $t = 0$ the laser field has decayed and the transfer process is finished and field-free evolution sets in. In the beginning the state has negative parity, due to dipole selection rules with respect to parity. The dynamics of the state is governed by the energy difference between states φ_5^{P} and φ_5^{M} , which is the parity violating energy difference $\Delta_{\text{pv}}E$ in this level (compare Table 11). Thus

$$\chi(t) = \frac{1}{\sqrt{2}}(\varphi_5^{\text{P}} - \exp(-i2\pi\Delta_{\text{pv}}Et/h)\varphi_5^{\text{M}}) \quad (38)$$

Again, for simplicity, we omitted the irrelevant overall phase. After a time $t = \tau_{\text{pv}}/2 = h/(2\Delta_{\text{pv}}E)$, the state χ has evolved into

$$\chi(t=\tau_{\text{pv}}/2) = \frac{1}{\sqrt{2}}(\varphi_5^{\text{P}} + \varphi_5^{\text{M}}) \stackrel{\text{def}}{=} \varphi_5^+ \quad (39)$$

which describes a state of positive parity. Note that at all times the time-dependent probability density in space remains constant:

$$|\chi(t)|^2 = \frac{1}{2}(|\varphi_5^{\text{P}}|^2 - \exp(-i2\pi\Delta_{\text{pv}}Et/h)|\varphi_5^{\text{M}}|^2) \quad (40)$$

$$\Rightarrow |\chi(t)|^2 = \frac{1}{2}(|\varphi_5^{\text{P}}|^2 + |\varphi_5^{\text{M}}|^2 + 2 \cos(2\pi\Delta_{\text{pv}}Et/h) \underbrace{\varphi_5^{\text{P}} \varphi_5^{\text{M}}}_{=0}) \quad (41)$$

$$= \frac{1}{2}(|\varphi_5^{\text{P}}|^2 + |\varphi_5^{\text{M}}|^2) = |\varphi_5^+|^2, \quad \forall t \quad (42)$$

The parity of χ oscillates with a period of motion inversely proportional to $\Delta_{\text{pv}}E$:

$$\tau_{\text{pv}} = h/(\Delta_{\text{pv}}E) \quad (43)$$

This enables us to extract the magnitude of $\Delta_{\text{pv}}E$ from the dynamics of the parity change of χ . This can be realized by a third probe pulse (third arrow in Figure 21) exciting a high-lying state of well-defined parity. In the simulation, the converged averaged energy of the transition as a function of field-free evolution time was recorded and is proportional to the transition probability in a real experiment. Figure 26 shows the situation for probing to a state of negative parity. The transition

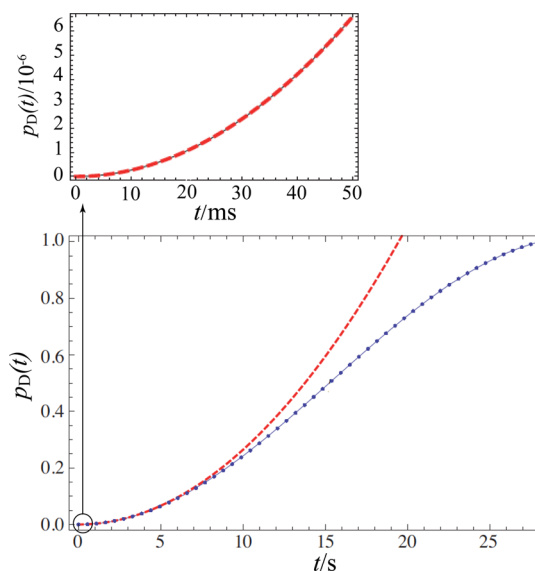


Figure 26. Transition probability as probability for detected states $p_{\text{D}}(t)$ as a function of free evolution time (full line) and the initially quadratic evolution (dashed). As soon as χ changes its parity, the transition probability increases. The total period is about 60 s; however, for high detection sensitivity, one could in principle measure the signal for a short time interval (top graph) and extract $\Delta_{\text{pv}}E$ from a fit according to eq 45.

is initially forbidden (due to parity selection rules) but becomes allowed as soon as the parity of χ changes. We can represent this fact by writing down the transition probability, which is the time-dependent probability for the detected state $p_{\text{D}}(t)$ as a function of $\Delta_{\text{pv}}E$ and field-free evolution time t :

$$p_{\text{D}}(t) = \sin^2(\pi\Delta_{\text{pv}}Et/h) \quad (44)$$

Because $\Delta_{\text{pv}}E$ is so small, the period of parity change is, in the case of Cl–O–O–Cl, several seconds. In a real experiment we may use a molecular beam to do the parity experiment in a collision-free environment. Still, we can reduce the interaction-free time needed for the measurement in cases where we have a high sensitivity of our detection set up. The initial time evolution in eq 44 is quadratic (dashed line in Figure 26, bottom):

$$p_{\text{D}}(t) \approx (\pi\Delta_{\text{pv}}Et/h)^2 \quad (45)$$

In the case of Cl–O–O–Cl we need to be able to record changes in transition probabilities of about 10^{-6} if we want to keep the interaction-free interval close to the millisecond time scales (Figure 26, top). From a fit of the experimentally recorded signal to eq 45, we could determine the absolute value of $\Delta_{\text{pv}}E$. In our case

$$\Delta_{\text{pv}}E = 5.5 \times 10^{-13} \text{ cm}^{-1} \quad (46)$$

is expected in accordance with Table 11.

In an actual experimental setup tested on ammonia, the sensitive detection of selected parity levels was achieved with an effective flight time of about 2 ms (flight path 0.8 m).^{109,110} The REMPI detection can essentially detect single ions generated, the sensitivity being in practice limited by the background signals.

4. CONCLUSION AND OUTLOOK

We presented a detailed numerical study of the stereomutation processes in a prototypical chiral molecule. We employed the

quasiadiabatic channel reaction path Hamiltonian method of solving the $3N - 6$ dimensional vibrational eigenvalue problem and combined the solution with a perturbative treatment of parity violation and an approximate treatment of the quantum dynamics under laser excitation. Cl–O–O–Cl acts also as prototypical molecule for the dynamics of an axially chiral molecule that shows tunneling switching for higher torsional excitations. Indeed, our calculations have shown a rich variety of interesting phenomena in the quantum dynamics of chiral molecules including electroweak parity violation and interaction with coherent laser fields.

The overall dynamics is governed by

1. The time evolution of molecular states under field-free conditions and including electroweak parity violation. Interconversion between enantiomers of chiral molecules can be due to tunneling stereomutation (TSM). Chiral states are unstable (fast tunneling motion), *de facto* stable (slow tunneling motion), or *de lege* stable (energetically stabilized due to parity violation, no tunneling motion),
2. The time evolution during laser interaction. Laser-induced stereomutation (LISM) can be achieved by an exciting laser field through population transfer between chiral and suitable intermediate states. Resonance Raman induced stereomutation (RRISM) is identified as a special case of LISM.

Depending on the time scales of TSM and laser interaction, both cases have to be accounted for when the quantum dynamics of excitation processes is studied.

We also presented a simple method to control population transfer in chiral molecules by introducing frequency-modulated or “chirped” laser pulses. Finally, we showed a simulation of a possible measurement of the parity violating energy difference $\Delta_{pv}E$ between enantiomers of chiral molecules based on probing time-dependent parity states.

In the future, further such experiments on stereomutation in chiral molecules could be investigated in the laboratory for prototypical molecules like H–O–O–H, H–S–S–H, and Cl–O–O–Cl and isotopomers with the help of a suitable laser setup and spectroscopy. The experiment to determine the parity violating energy difference directly was simulated for the case of Cl–O–O–Cl, which serves as theoretical proof of principle for such a measurement. The first successful experiments on population transfer with an appropriate experimental setup as a test on simple achiral molecules like acetylene or ammonia have been demonstrated.^{107,108,109}

Among the most significant results of the present investigation we should discuss the first complete simulation of the time-dependent quantum dynamics of chiral molecules under coherent laser irradiation with inclusion of the electroweak interaction and parity violation. Though these simulations are still approximate, they are perfectly realistic for a molecule that, in principle, would be suitable for carrying out the experiment to measure $\Delta_{pv}E$. Current limitations on available lasers make the experiments in the given frequency range not practical, though. Also, the theoretical values of $\Delta_{pv}E$ for Cl–O–O–Cl are relatively small, which would make such experiments for this molecule difficult although not impossible from this point of view.

Our calculations treat all internal degrees of freedom and rotation in a realistic, although approximate fashion. The quasiadiabatic channel reaction path approximation used here is clearly the most serious approximation. Rovibrational couplings

in the real molecule will change the detailed rovibrational dynamics appreciably. Even non-Born–Oppenheimer effects are much larger than the parity violating potentials. However, all these neglected effects are exactly symmetrical with respect to space inversion. Thus, they will not affect the fundamental aspects of the dynamics of time-dependent parity change relevant to the experiments, as these arise from antisymmetrical effects with respect to space inversion. Also, in principle, today the theoretical methods would be available to treat the quantum dynamics including coupling of all degrees of freedom for a molecule with just four atoms, as has been demonstrated for H–O–O–H and NH₃ and their isotopomers, for example, in refs 83, 111, and 112.

The simulations of population transfer in the present work are closely related to experiments already carried out in our laboratory on simpler test molecules,^{108,109} and further techniques for efficient quantum state selective population transfer are available as well.^{105,106,113}

Current and future work toward detecting molecular parity violation, following the route as outlined here in detailed simulations, concerns the selection of suitable molecules, which are accessible with currently available laser technologies. These will use excitation of strong transitions in the mid-infrared with lower laser powers (in the Watt range, using intensities below 1 kW/cm²).¹⁰⁹ Some success in the search for such molecules has been achieved, although they are of higher complexity than Cl–O–O–Cl.^{114,115} Nevertheless, the present theoretical simulations, the currently available experiments, and new molecular systems make the outlook for successful experiments promising. In the future, such experiments at high precision, combined with appropriate theoretical analysis, could provide information on the fundamental aspects of the standard model of particle physics (SMPP) complementary to results from high-energy physics.¹⁰

■ APPENDIX

In the Supporting Information (as electronic document) we provide the new program package used for our computations, as briefly summarized here. This had as a starting point our previous work.^{62,67,87} A comparison of the old RPH program package adapted for very small tunneling splittings from refs 62 and 87 with the current version from ref 68 is shown in Figure 27.

In the first step, the *ab initio* data are fitted to a trigonometric series in the new version compared to a spline interpolation of the data in the previous version. The new version has the advantage that small deviations and numerical “noise” due to limited precision in the *ab initio* calculations along the path can be easily accommodated and corrected. However, the disadvantage is that the topology of the potential has to be known *a priori*. In the case of torsional problems the potentials, etc. have to be periodic; therefore, a fit to a Fourier sin or cos series is possible. For other cases a polynomial expansion may be used.

Another advantage is that derived quantities such as harmonic wavenumbers can be tested for the right symmetry with respect to torsion. The symmetry could be enforced in the new version, whereas in the old version a filtering of the total sum potential is carried out at the end of the calculation.

The new calculations need almost a factor of 5 less in grid size to show convergence for the smallest tunneling splittings. Detailed discussion of differences in eigenenergies are given in section 2.1. Although the improvements are clearly significant

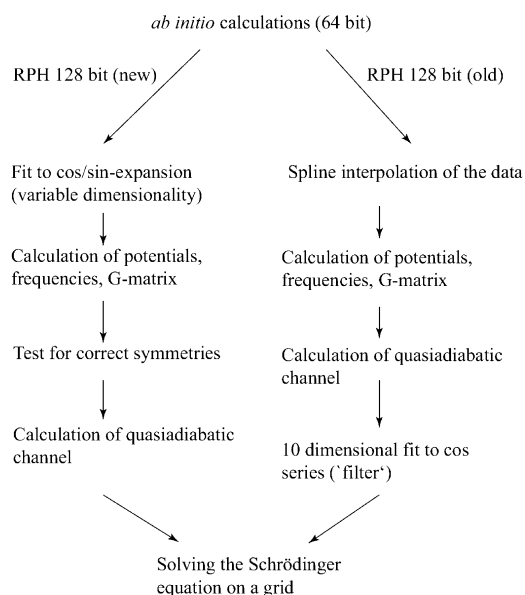


Figure 27. Comparison of the major routines in the existing and modified version of the RPH program used for calculating small tunneling splittings. In the newest version, the fit to sin/cos series takes place after the *ab initio* data are calculated, whereas in the old version the data get filtered at the last stage of the RPH calculation. Details of the program are available in the [Supporting Information](#).

numerically, they have no influence on the basic physics and discussions of ref 62, because of the extremely small values for tunneling splittings in those ranges, where the difference between the results are large in a relative sense, but still very small absolutely. The program is made available electronically in the [Supporting Information](#).

■ ASSOCIATED CONTENT

Supporting Information

The Supporting Information is available free of charge on the ACS Publications website at DOI: [10.1021/acs.jpca.5b08958](https://doi.org/10.1021/acs.jpca.5b08958).

RPH-program package consisting of FORTRAN codes, compilation- and execution-scripts; documentation; input files; exemplary output (PDF)

■ AUTHOR INFORMATION

Corresponding Authors

*R. Prentner. E-mail: robert.prentner@phil.gess.ethz.ch.

*M. Quack. E-mail: martin@quack.ch.

Notes

The authors declare no competing financial interest.

■ ACKNOWLEDGMENTS

We thank Sieghard Albert, Peter Dietiker, Csaba Fábri, L'uboš Horný, Eduard Miloglyadov, Georg Seyfang, and Fatih Ünlü for helpful discussions. Our work is supported financially by ETH Zürich, Schweizerischer Nationalfonds, and the European Research Council by an Advanced Grant and in the context of the COST project MOLIM. The calculations have been carried out on ETH's HPC cluster Brutus. In particular, the research leading to these results has received funding from the European Research Council under the European Union's Seventh Framework program (FP7/2007-2013) ERC Grant No. 280925. Help from Ruth Schüpbach is gratefully acknowledged.

■ REFERENCES

- (1) Van't Hoff, J. H. *La chimie dans l'espace*; P. M. Bazendijk: Rotterdam, 1887 (reprinted with commentary in ref 2).
- (2) Bourgois, C. Ed., Werner, A.; Pasteur, L.; van't Hoff, J. H. *Recherches sur la dissymétrie moléculaire (1860–1883)*; Collection Epistème: Dole, France, 1986.
- (3) Van't Hoff, J. H. *Vorlesungen über theoretische und physikalische Chemie. Zweites Heft: Die chemische Statik*; Vieweg: Braunschweig, 1899.
- (4) Fischer, E. Einfluss der Configuration auf die Wirkung der Enzyme. *Ber. Dtsch. Chem. Ges.* **1894**, *27*, 2985–2993.
- (5) Prelog, V. Chirality in Chemistry. In *Les prix Nobel en 1975*; Nobel Lectures; 1975.
- (6) Quack, M. The Concept of Law and Models in Chemistry. *European Review* **2014**, *22*, S50.
- (7) Hund, F. Zur Deutung der Molekelspektren. III. Bemerkungen über das Schwingungs- und Rotationspektrum bei Molekeln mit mehr als zwei Kernen. *Z. Phys.* **1927**, *43*, 805–826.
- (8) Quack, M. Structure and Dynamics of Chiral Molecules. *Angew. Chem., Int. Ed. Engl.* **1989**, *28*, 571–586.
- (9) Quack, M. Molecular Spectra, Reaction Dynamics, Symmetries and Life. *Chimia* **2003**, *57*, 147–160.
- (10) Quack, M. Fundamental Symmetries and Symmetry Violations. In *Handbook of High-Resolution Spectroscopy*; Quack, M., Merkt, F., Eds.; John Wiley: Chichester, U.K., 2011; Vol. 1, Chapter 18, pp 659–722.
- (11) Albert, S.; Quack, M. High Resolution Rovibrational Spectroscopy of Chiral and Aromatic Compounds. *ChemPhysChem* **2007**, *8*, 1271–1281.
- (12) Quack, M.; Stohner, J.; Willeke, M. High-resolution Spectroscopic Studies and Theory of Parity Violation in Chiral Molecules. *Annu. Rev. Phys. Chem.* **2008**, *59*, 741–769.
- (13) Patterson, D.; Schnell, M.; Doyle, J. M. Enantio-specific Detection of Chiral Molecules via Microwave Spectroscopy. *Nature* **2013**, *497*, 475–477.
- (14) Frank, P.; Bonner, W. A.; Zare, R. N. On One Hand But Not The Other: The Challenge of the Origin and Survival of Homochirality in Prebiotic Chemistry. In *Chemistry for the 21st Century*; Keinan, E., Schechter, I., Eds.; Wiley: Weinheim, 2001; pp 175–208.
- (15) Quack, M. How Important is Parity Violation for Molecular and Biomolecular Chirality? *Angew. Chem., Int. Ed.* **2002**, *41*, 4618–4630.
- (16) Meierhenrich, U. *Amino Acids and the Asymmetry of Life: Caught in the Act of Formation*; Springer: Berlin, 2008.
- (17) Jortner, J. Conditions for the Emergence of Life on the Early Earth: Summary and Reflections. *Philos. Trans. R. Soc., B* **2006**, *361*, 1877–1891.
- (18) Quack, M. On Biomolecular Homochirality as a Quasi-Fossil of the Evolution of Life. *Adv. Chem. Phys.* **2014**, *157*, 244–290.
- (19) Lin, G.-Q., You, Q.-D., Cheng, J.-F., Eds. *Chiral Drugs: Chemistry and Biological Action*; Wiley: Hoboken, NJ, 2011.
- (20) Shapiro, M.; Brumer, P. *Quantum Control of Molecular Processes. Second, Revised and Enlarged ed.*; Wiley-VCH: Weinheim, 2012.
- (21) González, L.; Hoki, K.; Kröner, D.; Leal, A. S.; Manz, J.; Ohtsuki, Y. Selective Preparation of Enantiomers by Laser Pulses: From Optimal Control to Specific Pump and Dump Transitions. *J. Chem. Phys.* **2000**, *113*, 11134–11142.
- (22) Lee, T.; Yang, C. Question of Parity Conservation in Weak Interactions. *Phys. Rev.* **1956**, *104*, 254–258.
- (23) Wu, C.; Ambler, E.; Hayward, R.; Hoppes, D.; Hudson, R. Experimental Test of Parity Conservation in Beta Decay. *Phys. Rev.* **1957**, *105*, 1413–1415.
- (24) Friedman, J. I.; Telegdi, V. L. Nuclear Emulsion Evidence for Parity Nonconservation in the Decay Chain $\pi^+ \rightarrow \mu^+ \rightarrow e^+$. *Phys. Rev.* **1957**, *105*, 1681–1682.
- (25) Garwin, R. L.; Lederman, L. M.; Weinrich, M. Observations of the Failure of Conservation of Parity and Charge Conjugation in Meson Decays: The Magnetic Moment of the Free Muon. *Phys. Rev.* **1957**, *105*, 1415–1417.

- (26) Glashow, S. L. Partial-Symmetries of Weak Interactions. *Nucl. Phys.* **1961**, *22*, 579–588.
- (27) Weinberg, S. A Model of Leptons. *Phys. Rev. Lett.* **1967**, *19*, 1264–1266.
- (28) Salam, A. Weak and Electromagnetic Interactions. In *Elementary Particles Theory: Relativistic Groups and Analyticity. Proceedings of the 8th Nobel Symposium held May 19–25, 1968 at Aspenäsgränden, Lerum, in the Count of Älvsborg, Sweden*; Svartholm, N., Ed.; Almqvist & Wiksell: Stockholm, 1968; pp 367–377.
- (29) Veltman, M. J. G. Nobel Lecture: From Weak Interactions to Gravitation. *Rev. Mod. Phys.* **2000**, *72*, 341–349.
- (30) 't Hooft, G. Nobel Lecture: A Confrontation with Infinity. *Rev. Mod. Phys.* **2000**, *72*, 333–339.
- (31) Yamagata, Y. A Hypothesis for the Asymmetric Appearance of Biomolecules on Earth. *J. Theor. Biol.* **1966**, *11*, 495–498.
- (32) Rein, D. W. Some Remarks on Parity Violating Effects of Intramolecular Interactions. *J. Mol. Evol.* **1974**, *4*, 15–22.
- (33) Letokhov, V. S. On Difference of Energy Levels of Left and Right Molecules Due to Weak Interactions. *Phys. Lett. A* **1975**, *53*, 275–276.
- (34) Hegström, R. A.; Rein, D. W.; Sandars, P. G. H. Calculation of the Parity Nonconserving Energy Difference Between Mirrorimage Molecules. *J. Chem. Phys.* **1980**, *73*, 2329–2341.
- (35) Mason, S. F.; Tranter, G. E. The Parity-violating Energy Difference Between Enantiomeric Molecules. *Mol. Phys.* **1984**, *53*, 1091–1111.
- (36) Bouchiat, M. A.; Bouchiat, C. Weak Neutral Currents in Atomic Physics. *J. Phys. (Paris)* **1974**, *35*, 899–927.
- (37) Bouchiat, M. A.; Bouchiat, C. Parity Violation Induced by Weak Neutral Currents in Atomic Physics. Part II. *J. Phys. (Paris)* **1975**, *36*, 493–509.
- (38) Conti, R.; Bucksbaum, P.; Chu, S.; Commins, E.; Hunter, L. Preliminary Observation of Parity Nonconservation in Atomic Thallium. *Phys. Rev. Lett.* **1979**, *42*, 343–346.
- (39) Bennett, S. C.; Wieman, C. E. Measurement of the $6S \rightarrow 7S$ Transition Polarizability in Atomic Cesium and an Improved Test of the Standard Model. *Phys. Rev. Lett.* **1999**, *82*, 2484–2487.
- (40) Shabaev, V. M.; Pachucki, K.; Tupitsyn, I.; Yerokhin, V. A. QED Corrections to the Parity-Nonconserving $6s-7s$ Amplitude in ^{133}Cs . *Phys. Rev. Lett.* **2005**, *94*, 213002.
- (41) Tsigutkin, K.; Dounas-Frazer, D.; Family, A.; Stalnaker, J. E.; Yashchuk, V. V.; Budker, D. Observation of a Large Atomic Parity Violation Effect in Ytterbium. *Phys. Rev. Lett.* **2009**, *103*, 071601.
- (42) Bakasov, A.; Ha, T.; Quack, M. Ab Initio Calculation of Molecular Energies Including Parity Violating Interactions. In *Chemical Evolution, Physics of the Origin and Evolution of Life, Proc. of the 4th Trieste Conference (1995)*; Chela-Flores, J., F. Raulin, F., Eds.; Kluwer: Dordrecht, The Netherlands, 1996; pp 287–296.
- (43) Lazzaretti, P.; Zanasi, R. On the Calculation of Parity-Violating Energies in Hydrogen Peroxide and Hydrogen Disulphide Molecules Within the Random-phase Approximation. *Chem. Phys. Lett.* **1997**, *279*, 349–354.
- (44) Bakasov, A.; Ha, T.; Quack, M. Ab Initio Calculation of Molecular Energies Including Parity Violating Interactions. *J. Chem. Phys.* **1998**, *109*, 7263–7285.
- (45) Bakasov, A.; Quack, M. Representation of Parity Violating Potentials in Molecular Main Chiral Axes. *Chem. Phys. Lett.* **1999**, *303*, 547–557.
- (46) Laerdahl, J. K.; Schwerdtfeger, P. Fully Relativistic *Ab Initio* Calculations of the Energies of Chiral Molecules Including Parity-violating Weak Interactions. *Phys. Rev. A: At., Mol., Opt. Phys.* **1999**, *60*, 4439–4453.
- (47) Berger, R.; Quack, M. Multiconfiguration Linear Response Approach to the Calculation of Parity Violating Potentials in Polyatomic Molecules. *J. Chem. Phys.* **2000**, *112*, 3148–3158.
- (48) Quack, M.; Stohner, J. Influence of Parity Violating Weak Nuclear Potentials on Vibrational and Rotational Frequencies in Chiral Molecules. *Phys. Rev. Lett.* **2000**, *84*, 3807–3810.
- (49) Laerdahl, J. K.; Schwerdtfeger, P.; Quiney, H. M. Theoretical Analysis of Parity-Violating Energy Differences Between the Enantiomers of Chiral Molecules. *Phys. Rev. Lett.* **2000**, *84*, 3811–3814.
- (50) Horný, L.; Quack, M. Computation of Molecular Parity Violation Using the Coupled-cluster Linear Response Approach. *Mol. Phys.* **2015**, *113*, 1768–1779.
- (51) Kompanets, O. N.; Kukudzhinov, A. R.; Letokhov, V. S.; Gervits, L. L. Narrow Resonances of Saturated Absorption of the Asymmetrical Molecule CHFClBr and the Possibility of Weak Current Detection in Molecular Physics. *Opt. Commun.* **1976**, *19*, 414–416.
- (52) Arimondo, E.; Glorieux, P.; Oka, T. Observation of Inverted Infrared Lamb Dips in Separated Optical Isomers. *Opt. Commun.* **1977**, *23*, 369–372.
- (53) Harris, R. A.; Stodolsky, L. Quantum Beats in Optical Activity and Weak Interactions. *Phys. Lett. B* **1978**, *78*, 313–317.
- (54) Quack, M. On the Measurement of the Parity Violating Energy Difference Between Enantiomers. *Chem. Phys. Lett.* **1986**, *132*, 147–153.
- (55) Pepper, M. J. M.; Shavitt, I.; v. Ragué Schleyer, P.; Glukhotsev, M. N.; Janoschek, R.; Quack, M. Is the Stereomutation of Methane Possible? *J. Comput. Chem.* **1995**, *16*, 207–225.
- (56) Bauder, A.; Beil, A.; Luckhaus, D.; Müller, F.; Quack, M. Combined High Resolution Infrared and Microwave Study of Bromochlorofluoromethane. *J. Chem. Phys.* **1997**, *106*, 7558–7570.
- (57) Daussy, C.; Marrel, T.; Amy-Klein, A.; Nguyen, C.; Border, C.; Chardonnet, C. Limit on the Parity Nonconserving Energy Difference Between the Enantiomers of a Chiral Molecule by Laser Spectroscopy. *Phys. Rev. Lett.* **1999**, *83*, 1554–1557.
- (58) Schnell, M.; Küpper, J. Tailored Molecular Samples for Precision Spectroscopy Experiments. *Faraday Discuss.* **2011**, *150*, 33–49.
- (59) Tokunaga, S. K.; Stoeffler, C.; Auguste, F.; Shelkovich, A.; Daussy, C.; Amy-Klein, A.; Chardonnet, C.; Darquié, B. Probing Weak Force-induced Parity Violation by High-resolution Mid-infrared Molecular Spectroscopy. *Mol. Phys.* **2013**, *111*, 2363–2373.
- (60) Horný, L.; Quack, M. General Discussion. *Faraday Discuss.* **2011**, *150*, 152–154.
- (61) Fehrensens, B.; Luckhaus, D.; Quack, M. Mode Selective Stereomutation Tunneling in Hydrogen Peroxide Isotopomers. *Chem. Phys. Lett.* **1999**, *300*, 312–320.
- (62) Quack, M.; Willeke, M. Stereomutation Tunneling Switching Dynamics and Parity Violation in Chlorineperoxide Cl-O-O-Cl . *J. Phys. Chem. A* **2006**, *110*, 3338–3348.
- (63) Berger, R.; Gottselig, M.; Quack, M.; Willeke, M. Parity Violations Dominate the Dynamics of Dichlorinedisulfide. *Angew. Chem., Int. Ed.* **2001**, *40*, 4195–4198.
- (64) Albert, S.; Lerch, P.; Prentner, R.; Quack, M. The High-resolution Spectrum of the Torsional Mode of Phenol. *Angew. Chem., Int. Ed.* **2013**, *52*, 346–349.
- (65) Prentner, R.; Quack, M.; Stohner, J.; Willeke, M. General Discussion. *Faraday Discuss.* **2011**, *150*, 130–132.
- (66) Miller, W. H.; Handy, N. C.; Adams, J. Reaction Path Hamiltonian for Polyatomic Molecules. *J. Chem. Phys.* **1980**, *72*, 99–112.
- (67) Fehrensens, B.; Luckhaus, D.; Quack, M. Inversion Tunneling in Aniline from High Resolution Infrared Spectroscopy and an Adiabatic Reaction Path Hamiltonian Approach. *Z. Phys. Chem.* **1999**, *209*, 1–19.
- (68) Prentner, R. Tunnelndynamik und Paritätsverletzung in chiralen und achiralen Molekülen. Diss. Nr. 20935. ETH Zürich, 2013.
- (69) Hofacker, L. Quantentheorie chemischer Reaktionen. *Z. Naturforsch., A: Phys. Sci.* **1963**, *18*, 607–619.
- (70) Marcus, R. A. Generalization of Activated Complex Theory of Reaction Rates. I. Quantum Mechanical Treatment. *J. Chem. Phys.* **1964**, *41*, 2614–2623.

- (71) Quack, M.; Troe, J. Specific Rate Constants of Unimolecular Processes. II. Adiabatic Channel Model. *Ber. Bunsenges. Phys. Chem.* **1974**, *78*, 240–252.
- (72) Quack, M.; Suhm, M. A. Quasiadiabatic Channels and Effective Transition-state Barriers for the Disrotatory In-plane Hydrogen-bond Exchange Motion in $(\text{HF})_2$. *Chem. Phys. Lett.* **1991**, *183*, 187–194.
- (73) Quack, M.; Troe, J. Statistical Adiabatic Channel Models. In *Encyclopedia of Computational Chemistry*; von Ragué Schleyer, P., Allinger, N. L., Clark, T., Gasteiger, J., Kollman, P. A., Schaefer, H. F., III, Schreiner, P. R., Eds.; Wiley: Chichester, U.K., 1998; Vol. 4, pp 2708–2726.
- (74) Podolsky, B. Quantum Mechanical Correct Form of Hamiltonian Function for Conservative Systems. *Phys. Rev.* **1928**, *32*, 812–816.
- (75) Watson, J. K. G. Simplification of the Molecular Vibration-rotation Hamiltonian. *Mol. Phys.* **1968**, *15*, 479–490.
- (76) Meyer, R.; Günthard, Hs. H. General Internal Motion of Molecules, Classical and Quantum-Mechanical Hamiltonian. *J. Chem. Phys.* **1968**, *49*, 1510–1520.
- (77) Lauvergnat, D.; Nauts, A. Exact Numerical Computation of a Kinetic Energy Operator in Curvilinear Coordinates. *J. Chem. Phys.* **2002**, *116*, 8560–8570.
- (78) Meyer, R. Trigonometric Interpolation Method for One-dimensional Quantum-mechanical Problems. *J. Chem. Phys.* **1970**, *52*, 2053–2059.
- (79) Luckhaus, D.; Quack, M. Spectrum and Dynamics of the CH Chromophore in CHD_2F . I. Vibrational Hamiltonian and Analysis of Rovibrational Spectra. *Chem. Phys. Lett.* **1992**, *190*, 581–599.
- (80) Bacic, Z.; Light, J. C. Theoretical Methods for Rovibrational States of Floppy Molecules. *Annu. Rev. Phys. Chem.* **1989**, *40*, 469–498.
- (81) Luckhaus, D. 6D Vibrational Quantum Dynamics: Generalized Coordinate Discrete Variable Representation and (A)diabatic Contraction. *J. Chem. Phys.* **2000**, *113*, 1329–1347.
- (82) Light, J. C.; Carrington, T., Jr. Discrete-Variable Representations and Their Utilization. *Adv. Chem. Phys.* **2000**, *114*, 263–310.
- (83) Fehrensen, B.; Luckhaus, D.; Quack, M. Stereomutation Dynamics in Hydrogen Peroxide. *Chem. Phys.* **2007**, *338*, 90–105.
- (84) Carrington, T. Using Iterative Methods to Compute Vibrational Spectra. In *Handbook of High-Resolution Spectroscopy*; Quack, M., Merkt, F., Eds.; John Wiley: Chichester, U.K., 2011; Vol. 1, Chapter 15, pp 573–585.
- (85) Tennyson, J. High Accuracy Rotation-Vibration Calculations on Small Molecules. In *Handbook of High-Resolution Spectroscopy*; Quack, M., Merkt, F., Eds.; John Wiley: Chichester, U.K., 2011; Vol. 1, Chapter 14, pp 551–571.
- (86) Császár, A. G.; Fábri, C.; Szidarovszky, T.; Mátyus, E.; Furtenbacher, T.; Czako, G. The Fourth Age of Quantum Chemistry: Molecules in Motion. *Phys. Chem. Phys.* **2012**, *14*, 1085–1106.
- (87) Gottselig, M.; Luckhaus, D.; Quack, M.; Stohner, J.; Willeke, M. Mode Selective Stereomutation and Parity Violation in Disulfane Isotopomers H_2S_2 , D_2S_2 , T_2S_2 . *Helv. Chim. Acta* **2001**, *84*, 1846–1861.
- (88) Frisch, M. J.; et al. *Gaussian 03*, Revision C.02; Gaussian, Inc.: Wallingford, CT, 2004.
- (89) Luckhaus, D.; Quack, M. The Far Infrared Pure Rotational Spectrum and the Coriolis Coupling Between ν_3 and ν_8 in $\text{CH}^{35}\text{ClF}_2$. *Mol. Phys.* **1989**, *68*, 745–758.
- (90) Watson, J. K. G. Aspects of Quartic and Septic Centrifugal Effects on Rotational Energy Levels. In *Vibrational Spectra and Structure*; Durig, J. R., Ed.; Elsevier: Amsterdam, 1978; Vol. 6, pp 1–89.
- (91) Quack, M.; Stohner, J. How do Parity Violating Weak Nuclear Interactions Influence Rovibrational Frequencies in Chiral Molecules? *Z. Phys. Chem.* **2000**, *214*, 675–703.
- (92) Quack, M.; Stohner, J. Molecular Chirality and the Fundamental Symmetries of Physics: Influence of Parity Violation on Rovibrational Frequencies and Thermodynamic Properties. *Chirality* **2001**, *13*, 745–753.
- (93) Quack, M.; Stohner, J. Combined Multidimensional Anharmonic and Parity Violating Effects in CDBrClF. *J. Chem. Phys.* **2003**, *119*, 11228–1240.
- (94) Hobi, F.; Berger, R.; Stohner, J. Investigation of Parity Violation in Nuclear Spin-Rotation Interaction of Fluorooxirane. *Mol. Phys.* **2013**, *111*, 2345–2362.
- (95) Quack, M. Theory of Unimolecular Reactions Induced by Monochromatic Infrared Radiation. *J. Chem. Phys.* **1978**, *69*, 1282–1307.
- (96) Quack, M. Reaction Dynamics and Statistical Mechanics of the Preparation of Highly Excited States by Intense Infrared Radiation. *Adv. Chem. Phys.* **1982**, *50*, 395–473.
- (97) Quack, M.; Sutcliffe, E. On the Validity of the Quasiresonant Approximation for Molecular Infrared-multiphoton Excitation. *J. Chem. Phys.* **1985**, *83*, 3805–3812.
- (98) Quack, M.; Stohner, J. Femtosecond Quantum Dynamics of Functional Groups under Coherent Infrared Multiphoton Excitation as Derived from the Analysis of High-resolution Spectra. *J. Phys. Chem.* **1993**, *97*, 12574–12590.
- (99) Stohner, J. Theoretische Untersuchungen zur Quantendynamik der Infrarotvielfotonenanregung des CH Chromophors in vielatomigen Molekülen geringer Symmetrie. Diss. Nr. 10701. ETH Zürich, 1994.
- (100) Quack, M. Multiphoton Excitation. In *Encyclopedia of Computational Chemistry*; von Ragué Schleyer, P., Allinger, N. L., Clark, T., Gasteiger, J., Kollman, P. A., Schaefer, H. F., III, Schreiner, P. R., Eds.; Wiley: Chichester, U.K., 1998; Vol. 3, pp 1775–1791.
- (101) Merkt, F.; Quack, M. Molecular Quantum Mechanics and Molecular Spectra, Molecular Symmetry, and Interaction of Matter with Radiation. In *Handbook of High-Resolution Spectroscopy*; Quack, M., Merkt, F., Eds.; John Wiley: Chichester, U.K., 2011; Vol. 1, Chapter 1, pp 1–55.
- (102) Marquardt, R.; Quack, M.; Thanopoulos, I. Dynamical Chirality and the Quantum Dynamics of Bending Vibrations of the CH Chromophore in Methane Isotopomers. *J. Phys. Chem. A* **2000**, *104*, 6129–6149.
- (103) Marquardt, R.; Quack, M. Radiative Excitation of the Harmonic Oscillator with Applications to Stereomutation in Chiral Molecules. *Z. Phys. D: At., Mol. Clusters* **1996**, *36*, 229–237.
- (104) Loy, M. M. T. Observation of Population Inversion by Optical Adiabatic Rapid Passage. *Phys. Rev. Lett.* **1974**, *32*, 814–817.
- (105) Liedenbaum, C.; Stolte, S.; Reuss, J. Inversion Produced and Reversed by Adiabatic Passage. *Phys. Rep.* **1989**, *178*, 1–24.
- (106) Vitanov, N. V.; Halfmann, Th.; Shore, B. W.; Bergmann, K. Laser-induced Population Transfer by Adiabatic Passage Techniques. *Annu. Rev. Phys. Chem.* **2001**, *52*, 763–811.
- (107) Ünlü, F. Zum Aufbau eines spektroskopischen Experiments zur Bestimmung der paritätsverletzenden Energiedifferenz zwischen Enantiomeren chiraler Moleküle: Doppelresonanzexperimente zur effizienten Population von Paritätszuständen. Diss. Nr. 19828. ETH Zürich, 2011.
- (108) Dietiker, P.; Quack, M.; Schneider, A.; Seyfang, G.; Ünlü, F. IR-Laser Induced Population Transfer from Highly Populated Rotational Levels of NH_3 in a Molecular Beam. In *Contributions, 18th Symposium on Atomic and Surface Physics and Related Topics, Alpe d'Huez, France, 22. to 27. January 2012*; Lewerenz, M., Dutuit, O., Marquardt, R., Eds.; Innsbruck University Press: Innsbruck, 2012; pp 263–267.
- (109) Dietiker, P.; Miloglyadov, E.; Quack, M.; Schneider, A.; Seyfang, G. Two Photon IR-Laser Induced Population Transfer in NH_3 : First Steps to Measure Parity Violation in Chiral Molecules. In *Contributions, 18th Symposium on Atomic and Surface Physics and Related Topics, Obergurgl, Austria, 8. to 14. February 2014*; Stock, D., Wester, R., Scheier, P., Eds.; Innsbruck University Press: Innsbruck, 2014; pp 226–229 (and *J. Chem Phys.* **2015**, *143*, in press).
- (110) Hippler, M.; Miloglyadov, E.; Quack, M.; Seyfang, G. Mass and Isotope Selective Infrared Spectroscopy. In *Handbook of High-Resolution Spectroscopy*; Quack, M., Merkt, F., Eds.; John Wiley: Chichester, U.K., 2011; Vol. 2, Chapter 28, pp 1069–1118.

(111) Marquardt, R.; Sagui, K.; Zheng, J.; Thiel, W.; Luckhaus, D.; Yurchenko, S.; Mariotti, F.; Quack, M. Global Analytical Potential Energy Surface for the Electronic Ground State of NH_3 from High Level ab Initio Calculations. *J. Phys. Chem. A* **2013**, *117*, 7502–7522.

(112) Fábri, C.; Marquardt, R.; Quack, M. Full-dimensional Quantum Dynamics and Spectroscopy of Ammonia Isotopomers. *Chimia* **2014**, *68*, CC-021.

(113) Dong, W.; Mukherjee, N.; Zare, R. N. Optical Preparation of H_2 Rovibrational Levels with Almost Complete Population Transfer. *J. Chem. Phys.* **2013**, *139*, 074204.

(114) Fábri, C.; Horný, L.; Quack, M. Tunneling and Parity Violation in Trisulfane (HSSH): An Almost Ideal Molecule for Detecting Parity Violation in Chiral Molecules. *ChemPhysChem* **2015**, *16*, 3584–3589, DOI: [10.1002/cphc.201500801](https://doi.org/10.1002/cphc.201500801).

(115) Albert, S.; Bolotova, I.; Chen, Z.; Fábri, C.; Horný, L.; Seyfang, G.; Zindel, D.; Quack, M. High Resolution Infrared Spectroscopy and Theory of Parity Violation and Tunneling for Dithiine as a Candidate for Measuring the Parity Violating Energy Difference Between Enantiomers of Chiral Molecules. *Chimia* **2015**, *69*, PC-015.